Modeling of Resolution of X-Ray Imaging Detectors

Wenyuan Shen

A Thesis

In the Department

of

Electrical and Computer Engineering

Presented in Partial Fulfillment of the Requirements

for the Degree of Master of Applied Science at

Concordia University

Montréal Québec Canada

December 2009

Your file Votre référence
ISBN: 978-0-494-67136-8
Our file Notre référence
ISBN: 978-0-494-67136-8

ABSTRACT

Modeling of Resolution of X-ray Imaging Detectors

Wenyuan Shen

A flat-panel detector based on a photoconductive detector with an active matrix array provides superior x-ray images. Amorphous selenium (a-Se) is currently the best choice of photoconductor for clinical x-ray image detectors.

Spatial resolution in terms of modulation transfer function (MTF) is an important metric to examine the image quality of a detector. Based on current understanding for diagnostic energy x-rays, the dominant mechanisms responsible for the loss of resolution are: charge carrier trapping, range of primary photoelectrons, and reabsorption of K-fluorescent x-ray photons. Any trapped carrier in the photoconductor layer induces charges not only on the corresponding pixel but also on the neighbouring pixels, and consequently there is a lateral spread of the signal. The absorption of x-ray in the photoconductor first creates a high energy photoelectron that creates hundreds of electron-hole pairs (EHP) along its arbitrary path. This creates an EHP cloud within a volume and destroys image resolution. Some of the K-fluorescent x-ray photons may be reabsorbed at different points within the detector which creates the loss of resolution.

In this thesis, a semi-analytical model for calculating MTF due to the reabsorption of K-fluorescent x-ray photons is proposed. A complete MTF model is proposed and it is evaluated as a function of material properties (carrier lifetime), detector thickness, x-ray photon energy and operating field applied. The analytical MTF model is compared with

the published experimental data on various x-ray detectors and shows very good agreement. The overall MTF model can be applied to other direct-conversion detectors such as HgI_2, PbO and CdZnTe x-ray image detectors as well.

To my loving parents

Shu'e & Konglong.

ACKNOWLEDGMENTS

In the first place, I am grateful for the support and help from my parents and they have been there for me for the whole time.

I would like to record my gratitude to Dr. M.Z. Kabir for his tireless help and guidance. This thesis would not be possible without his advice and supervision. I am thankful of my colleagues Mr. Asif Mahmood, Mr. Md Wasiur Rahman, and Md Shahnawaz Anjan for their useful discussions.

I also would like to show my gratitude to the professors and staff at Concordia University which includes: Diane Moffat, Tadeusz Obuchowicz, the ISO team members and Uchema Mgbemena.

Finally, I appreciate the help and encouragement from all my friends.

Contents

List of Figures

List of Tables

Chapter 1 Introduction

1.1 Radiography

Radiography is a method using x-rays to penetrate into an object in order to have a better view of the inside of the object. The birth of radiology happened more than 110 years ago. X-rays were first discovered by physicist Wilhelm Conrad Rontgen 1895, and 15 years later, he was honored with the Nobel Prize. The range of x-ray wave lengths for diagnostic medical imaging span is from 0.1nm (12.4keV) to 0.01nm (124keV).

Initially, when W.C. Rontgen discovered the rays, people called it "roentgen rays", but internationally the term x-rays was used since W.C. Rontgen named the rays mystery or x-rays at the time he discovered them. At that time no one could predict the future of the usage of x-rays, especially in medical diagnostic imaging and therapies. In 1895, W.C. Rontgen took the first x-ray image of his wife's hand and entitled it "Hand with Rings." Within a month the first medical images were taken but the exposure time was up to one hour. Comparably, the exposure time today been reduced to within milliseconds, and the dosage used for radiography has been reduced by approximately 2% of what was previously required, and this mainly because of the introduction of the usage of digital radiography [1]. The discovery of x-rays leads to a big influence of medical diagnostic images and therapies. During the last 100 years radiology and medical imaging have experienced a rapid development. Nowadays, x-rays are used in 70% of radiographic diagnoses [1] [2].

1.2 Radiographic Imaging

X-rays are indeed a form of electromagnetic radiation, and the attenuations of the electromagnetic radiation vary according different tissues and structures inside the patients. Traditionally, radiographic images are taken on film. Radiographers take the radiograph of the patient on a cassette film for the radiologist to diagnose. Patients are placed in between the x-ray source and the detector and after the x-rays pass through the patient with different attenuations, they reach the detector. The detector consists of a cassette film held right behind the phosphor screen. Therefore when the exposure is taking place, the screen gives off the light which exposes the film and leaves the image which can be seen after the development. The film-based analog radiography was urged to be replaced by newer technology because of its drawbacks: long exposure, inefficiency, and high dosage. Therefore interests have been made in the development of digital radiographic systems. In a digital radiographic system, the place where the cassette film was placed is replaced by a digital image capture device in order to record the x-ray image. Comparing to film-based analog radiography, the benefits of digital radiographic systems are: improvement of image portability; reduction of the exposure time and dose; increased efficiency in terms of storage and display, because instead of storing the images in cassette films, they can be easily stored on computer memory devices (such as hard drives), and the real-time images can be viewed by a radiologist on the monitor.

1.3 Flat-Panel Detectors

Instead of using cassette films in a conventional radiographic system, a flat-panel x-ray imaging detector is placed in a digital radiographic system. Usually, this flat-panel x-ray imaging detector contains active matrix arrays or thin-film transistor arrays. Flat-panel detectors with active matrix arrays are called active matrix flat-panel imagers (AMFPI). The cassette films in the conventional radiographic systems can be easily replaced by the AMFPI, and the x-ray images will be collected immediately after the exposure. The images are stored in a computer and displayed on a monitor, so they can be easily viewed and/or transited and/or stored for further use and diagnoses.

An AMFPI model is illustrated in Figure 1.1 [3]. The AMFPI is integrated within the detector. The AMFPI consists of many pixels, and each pixel acts individually as a detector itself. It collects the information from the radiation and then generates a certain amount of charge which corresponds to the amount of the radiation it receives. This information collection and charge production process can be performed by two different approaches which have been used to categorize the flat-panel x-ray imaging detectors. They are indirect and direct conversion detectors, and will be explained in detail in the following sections.

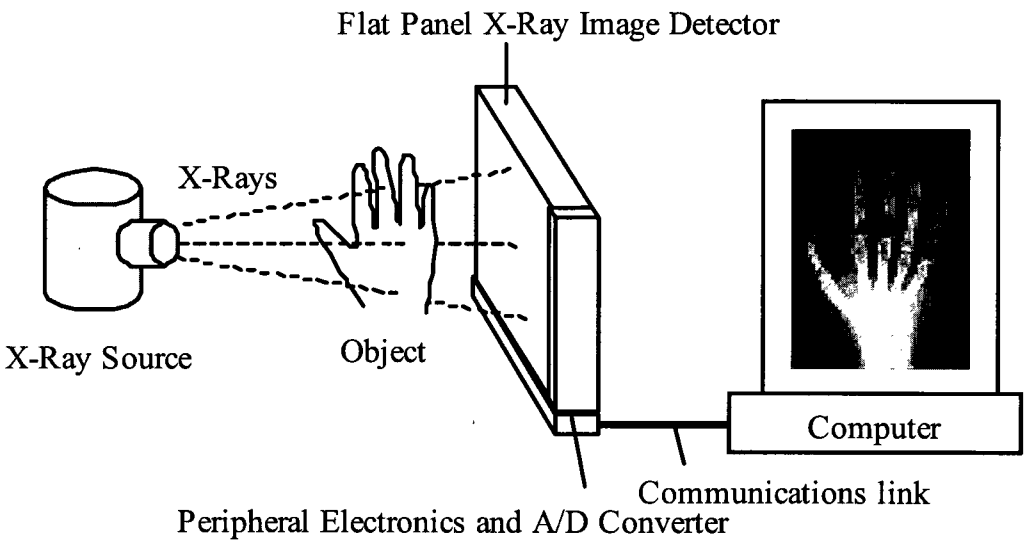

Figure 1.1 Schematic illustration of an AMFPI system [3].

Indirect-conversion detectors are used to replace the cassette films and have been used by several manufactures and research institutions. An indirect-conversion detector consists of a phosphor screen and a photodiode. The phosphor screen converts x-ray photons into visible lights and then they are absorbed by the photodiode. Inside the photodiode, electron-hole pairs (EHPs) are created and collected by the pixels. This type of detectors helped to digitalize radiography, but comparing to indirect-conversion detector, direct-conversion detectors provide superior image quality, less cost and are simpler to manufacture due to the structure of the detectors. These superior advantages have made the direct conversion detectors become a major solution for digital radiography [4] [5].

Direct-conversion method is one of the most widely used approaches for digital radiography which provides superior x-ray images, and many energies and efforts have been made to improve the technology by scientists during the last few decades. Figure 1.2

shows a photograph of a direct-conversion flat-panel x-ray imaging detector, and it has a amorphous Selenium photoconductor.

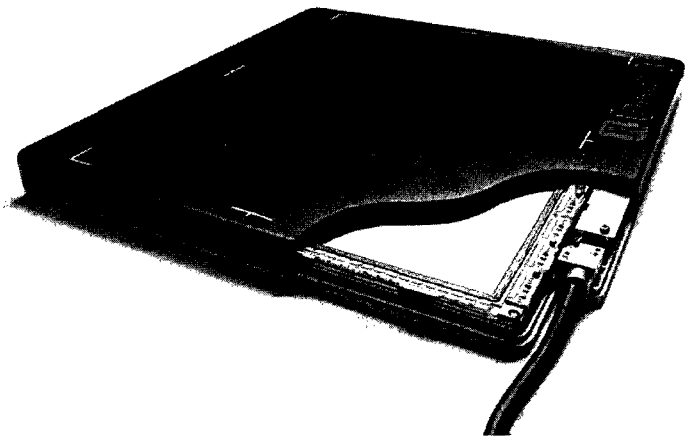

Figure 1.2 A direct-conversion flat-panel x-ray imaging detector with active matrix arrays. (Courtesy of Direct Radiography Corp.).

The structure of a direct conversion detector is similar to that of a indirect conversion detector. However the most obvious difference between them is that there is no phosphor in a direct conversion detector, and a photodiode is replaced by a photoconductor. A simplified schematic diagram of the cross-sectional structure of a two pixels direct-conversion flat-panel self-scanned x-ray imaging detector is shown in Figure 1.3 [6].

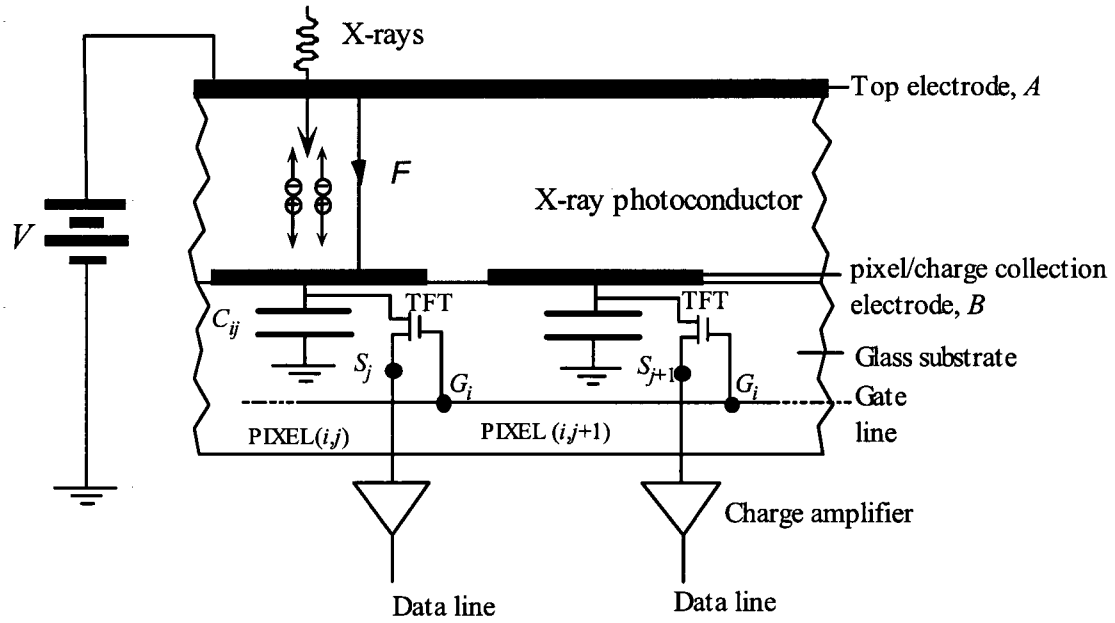

(a)

Figure 1.3 A simplified schematic diagram of the cross-sectional structure of a two pixels direct-conversion flat-panel self-scanned x-ray image detector [6].

A photoconductor is sandwiched in between two electrodes, and the top electrode is negatively biased. The bias polarity can be negative or positive. The top electrode is a continuous metal plate and bottom electrode is segmented into individual square pixels. At the bottom electrode, as shown in Figure 1.3, there are two pixels and both of them are connected to a capacitor which will be used to store the charges collected at the bottom electrode. As well as the capacitor, a thin-film transistor (TFT) is connected to each pixel and amplifier. Each TFT has three terminals: the gate terminal is connected to the gate line controlled by the scan unit, and it gives the "command" when the TFT is "ON" or

"OFF"; the drain terminal is associated to the bottom pixel electrode and a capacitor; the source terminal is connected to the amplifier which is connected to the data line.

Incoming x-ray photons penetrate into the photoconductor in the direction of the bottom electrode, and on the path of x-ray photons electron-hole pairs (EHPs) are generated by absorbing the energy of x-ray photons inside the photoconductor. If we apply a negative bias (could vary from hundreds to thousands volts) on the top electrode, the electric field lines are towards the top electrode (the capacitance of the photoconductor over the pixel is much smaller than the pixel capacitance). The electrons and holes will be drifted along the electric field lines. Holes are collected at the negative biased electrode on the top of the photoconductor and on the other hand, electrons are accumulated in the storage capacitors which are connected to the bottom pixel electrode. The amount of charges collected at a pixel is proportional to the amount of x-ray photons absorbed inside the detector above the pixel. To read out the image, the TFT is turned on by a scanning unit every few seconds, and the information-charge signals stored in the capacitor are transferred to the data line and then to the charge amplifier. These signals are sent to a multiplexer to be digitalized and fed into a computer system for storage and display. The photography of an a-Se based direct-conversion flat-panel active matrix x-ray imaging detector is shown in Figure 1.4.

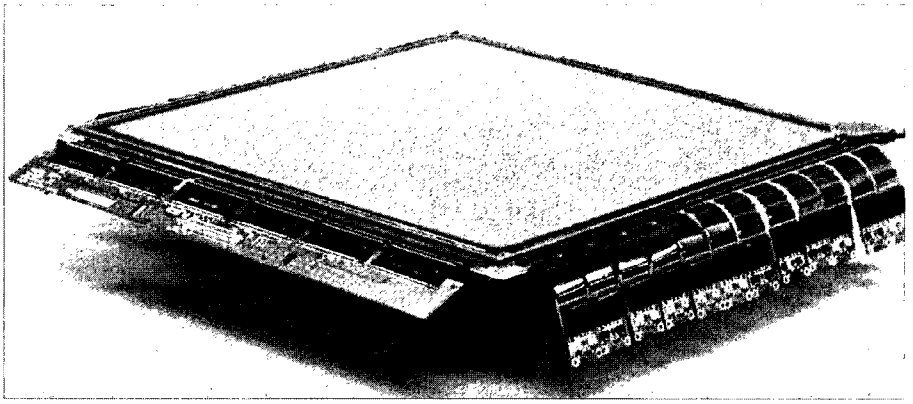

Figure 1.4 An a-Se based direct-conversion flat-panel active matrix x-ray imaging detector (Courtesy of ANRAD Corp.).

1.4 Active Readout Matrix

Generally, an active readout matrix consists of rows and columns of storage capacitors which are connected to the thin-film transistors (TFTs). To read the information stored in the capacitors, TFTs are turned on by the scanning control unity and then the charges are transferred from the capacitors through the TFTs and converted into digital signals by a multiplexer [7].

A schematic diagram of a 3X3 active matrix array is shown in Figure 1.5 [4]. On row i, all the gates of the TFTs are connected to the same gate control line to the scanning control unit, and on column j, all the source terminals of the TFTs are connected to the same data line which passes the signals from the capacitors to the multiplexer. When the gates of TFTs of row i are activated, TFTs are at "ON" state, and data lines will transfer the signals from the pixels on row i of column j-1, j and j+1 to the multiplexer individually. Next, the gates of TFTs of row i+1 are activated and the signals are transferred, and the process is repeated until the signals from all pixels are transferred to

the multiplexer. The image is captured by this method and by the end of the process the system is ready for another exposure.

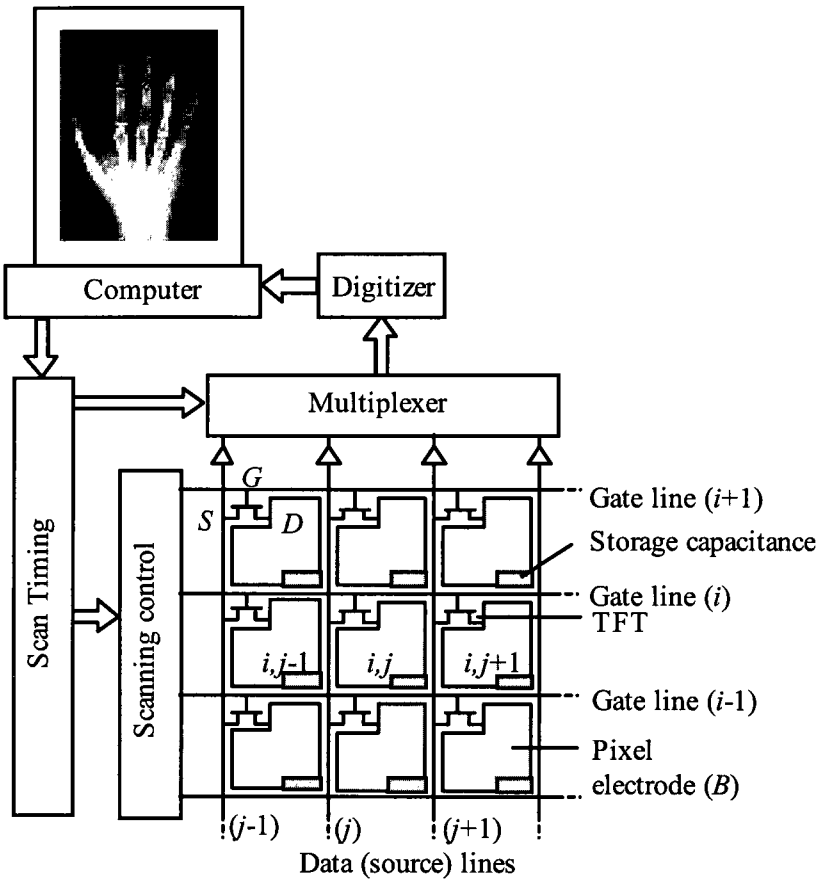

Figure 1.5 A schematic diagram of a 3X3 active matrix array of an x-ray imaging detector system [4].

1.5 General Requirements

A direct-conversion flat-panel x-ray imaging detector can be used in various radiographies, including: chest radiology [8] [9], mammography and fluoroscopy [10] [11] [12]. For different purposes there are different requirements for the imaging systems. The general requirements of an x-ray imaging detector system for chest radiology, mammography and fluoroscopy are listed in Table 1.1 [13].

Table 1.1 General parameters of an x-ray imaging system for different applications are listed below and for various situations those parameters vary. In the table, kVp is the peak value of the voltage applied to the x-ray tube for generating x-rays, R(Rontgens) is the unit of x-ray exposure [13].

	Chest Radiology	**Mammography**	**Fluoroscopy**
Detector Size (cm)	35 X 43	18 X 24	25 X 25
Pixel Size (μm)	200 X 200	50 X 50	250 X 250
Number of Pixels	1750 X 2150	3600 X 4800	1000 X 1000
Readout time (s)	~1	~1	~1/30
X-ray Spectrum (kVp)	120	30	70
Mean Exposure	300μR	12mR	1μR
Exposure Range	30-3000μR	0.6-240mR	0.1-10μR

1.6 Ideal X-ray Photoconductors

A direct-conversion flat-panel x-ray imaging detector system consists of many components. The core is the photoconductor where x-ray photons are absorbed and charges are created. The performance of the photoconductor mainly determines the performance of the digital x-ray imaging detector system, so the chosen material and the design of the photoconductor layer are very crucial, and identifying the important properties and characteristics are necessary. Ideally we expect the photoconductor to possess the following properties and characteristics [14]:

1. All the incident x-ray photons are absorbed within a certain depth which should be smaller than the thickness of the photoconductor in order to reduce the exposure time and the usage of the dose.
2. The materials used to manufacture the photoconductors are expected to have a high intrinsic x-ray sensitivity, which means that the photoconductor would generate as many collectable electron-hole pairs (EHPs) as possible. In other words, the amount of radiation energy required to generate the EHPs of the materials used to produce the photoconductor should be as low as possible. This will minimize unnecessary exposure to the patients.
3. EHPs are created inside the photoconductor and there is no bulk recombination as the charge carriers are drifted across the photoconductor, and even if there is a bulk recombination, it is negligible for medical radiography because of small signals used in this case. Bulk recombination is proportional to the square of concentration of EHPs.

4. To obtain a better image/spatial resolution, the diffusion of the carriers should be negligible compared to the drift by the electric field inside the photoconductor.
5. Deep trapping should be limited at a very low level to achieve an ideal photoconductor. The schubweg is the distance a carrier can travel before it is trapped by a deep trapping centre and it is defined as $\mu\tau F \gg L$, where μ is the drift mobility, τ is the lifetime of both carriers (electrons and holes), F is the electric field, and L is the thickness of the photoconductor.
6. As a source of noise, dark current should be limited as low as possible. In order to lower the dark current, the contacts of the photoconductor should be non-injecting and the generation rate of carriers from defects or states in the band gap should be substantially small. To minimize the conductivity of dark current, usually the materials used for the photoconductor should have a wide band gap, which conflicts with condition (2). Generally the dark current is preferably controlled within the range of 10-1000 pA/cm^2 [15].
7. Depending on the smallest drift mobility, the longest carrier transit time should be less than the period of the readout process of the pixels.
8. The properties of the photoconductors should remain the same the entire time, or the recovery of the damage should be very short in order to provide good imaging results continuously.
9. The properties and characteristics of the photoconductor should remain uniformed over the entire space.
10. The temporal artifacts (ghosting and lag) should be as small as possible.
11. The photoconductor itself should be easily attached/coated to active matrix arrays.

For most cases, it is hard to produce a large area photoconductor which is mainly limited by the coating requirement [16]. For instance, crystalline semiconductor materials are difficult to grow to a large area. On the contrary, amorphous and polycrystalline semiconductor materials [17] have better properties in terms of the size. Consequently, they are the best choices so far [18] [19]. Currently, amorphous-Selenium (a-Se) is one of the most commonly used photoconductor material for large area flat-panel x-ray imaging detectors [20]. In addition, it can be easily coated onto a substrate, and has smaller dark-current than polycrystalline-material photoconductors, acceptable x-ray absorption coefficient and good charge transport properties [4] [21]. However, the amount of radiation energy required to create an electron-hole pair (EHP) is about 45 eV in a-Se. Polycrystalline materials, such as poly-HgI_2 and poly-CdZnTe has much smaller ionization energy than amorphous materials, but they have their drawbacks due to the large grain size and higher dark-current.

So far, stabilized a-Se is the best choice of photoconductors for diagnostic purposes. However, other materials such as poly-HgI_2, CZT and PbO are very competitive materials for photoconductors as well. In this thesis, an effort has been made towards the a-Se based flat-panel x-ray imaging detectors.

1.7 Literary Review and Motivation

The rapid development of digital radiography technology makes radiography more accessible and efficient, thus better x-ray images are provided. Flat-panel x-ray imaging detectors have been found to be suitable for applying to large area digital imaging applications, and due to the advantages of direct-conversion method, efforts

have been made to develop a better direct-conversion flat-panel x-ray imaging detector system. One of the most important parts of direct-conversion x-ray imaging detector technology is the photoconductor where x-ray photons are absorbed and electrical charges are created. As mentioned before, the material used to manufacture a photoconductor should have a high intrinsic x-ray sensitivity, and so far amorphous selenium (a-Se) is one of the most commonly used materials for photoconductor because of its large band gap (2.2 eV, in large band gap material, bulk generated dark current can be neglected) [22]. Generally, a-Se photoconductor is operated with a high electric field (10V/μm) to ensure the x-ray sensitivity [23]. In this thesis, a-Se based flat-panel x-ray imaging detector is studied due to its own advantages and wide range applications.

Resolution in terms of modulation transfer function (MTF) is a very useful tool for describing and evaluating the spatial resolution of an x-ray image system [24]. The MTF is the relative response of the imaging system as a function of spatial frequency. Previously, MTFs due to different effects have been studied by other researchers. Que and Rowlands [25] discussed and evaluated the spatial resolution of a-Se based flat-panel x-ray imaging detector in terms of MTF, including the effect of primary photoelectrons, Compton scattering and reabsorption of K-fluorescent. Kabir and Kasap [26] proposed the MTF model due to the effect of charge carrier trapping. Recently, Kabir [27] proposed an analytical model for calculating the MTF due to the effect of primary photoelectrons. Based on the present understanding, the range of primary photoelectron, reabsorption of K-fluorescent x-ray photons, charge carrier trapping and aperture are the dominant mechanism for the loss of resolution in a direct-conversion x-ray imaging detector. However, a complete MTF model considering all the above effects is yet to be

developed. The overall MTF of an x-ray imaging system can be described as a cascade of several stages where the overall MTF is simply the product of the MTFs of all the individual stages.

In this thesis, the MTFs of amorphous-Selenium (a-Se) based direct-conversion flat-panel x-ray imaging detector system are evaluated individually, including the following components:

(1) Electron-hole pairs (EHPs) are created in the photoconductor by absorbing energy of initial x-ray photons, and those EHPs travel away from the initial interaction point within a certain range, which will degrade the resolution of the system. This incident is called photoelectric effect, thus a MTF model – $MTF_{pe\ is}$ used to evaluated the resolution loss;

(2) Photoelectric incident will leave vacancies in the atoms of the photoconductor, and this will lead to a cascade of atomic electron transitions in the atoms, and generate characteristic x-rays which is titled as K-fluorescent x-rays. They will be reabsorbed and generate more EHPs and this degrades the image resolution, thus MTF due to reabsorption of K-fluorescence – a simpler MTF_k is discussed and proposed.

(3) Charge carries are drifted along the electric lines toward the electrodes and collected at the bottom electrode by the pixels, but when the carriers are traveling inside the photoconductor, they will experience trapping by both shallow and deep trap centers, which degrades the resolution of the system. Thus, the MTF due to trapping – MTF_{trap} is calculated;

(4) MTF due to aperture – MTF_{ap} arises because of the average signals over a pixel area.

Therefore, giving an overall MTF model of an x-ray detector will help provide a better understanding of the x-ray image system and give guidance on how to improve the detector in order to minimize the x-ray exposure on the human body and maximize the quality of the x-ray images at the same time, so efforts have been made to develop an overall MTF model in this thesis.

1.8 Objectives

This thesis is concentrating on modulation/resolution transfer function (MTF) of amorphous-Selenium (a-Se) based direct conversion flat-panel x-ray image detector. The overall objectives consist of:

(1) Developing a simpler semi-analytical expression for calculating MTF due to the reabsorption of K-fluorescent x-ray photons;

(2) Determining the overall presampling MTF model considering the effects of primary photoelectrons traveling range, reabsorption of K-fluorescent x-ray photons, charge carrier trapping, and aperture;

(3) Examining the MTF model by applying it to the published experimental data and identifying the significant factors that limit the image resolution.

Although most of the calculations and examinations are based on a-Se based direct conversion flat-panel x-ray image detectors, the MTF model can be applied to other material based direct conversion detectors, such as HgI_2, PbO and CdZnTe x-ray image detectors [28] [29].

1.9 Thesis Outline

The thesis is divided into five chapters. This chapter introduces the basic knowledge of radiology, its history and development. The second chapter provides useful background theories and important terms of x-ray imaging detectors and Modulation Transfer Functions (MTFs). MTF due to the reabsorption of K-fluorescent x-ray and an overall MTF model of an amorphous-Selenium based direct-conversion flat-panel x-ray imaging detector system is presented in Chapter 3, and Chapter 4 gives the results and presents the discussions. Conclusions, contributions and future work are summarized in Chapter 5.

Chapter 2 Background Theories

2.1 Introduction

X-ray image detector related background theories are reviewed in this chapter, as well as important terms used for x-ray image systems. In addition, Modulation Transfer Functions of a direct-conversion flat-panel x-ray imaging detector system are introduced. The main parts of this chapter are: x-ray generation, x-ray interactions in a photoconductor, ionization energy properties of amorphous Selenium material, x-ray filtration and effective energy and modulation/resolution transfer functions.

2.2 X-ray Generation

2.2.1 Introduction

X-ray is a form of electromagnetic/ionizing radiation which is originated from the atomic level of an atom. X-rays can be generated by several different approaches, and two of the most commonly used methods are Bremsstrahlung and characteristic x-ray generation system.

2.2.2 Bremsstrahlung Radiation

Bremsstrahlung radiation means breaking radiation since Bremsstrahlung in German translates to "breaking radiation". Bremsstrahlung is defined as the process where photons are emitted in the scattering of electrons from atoms.

Generally, an energetic electron travels to the metal target with a high speed and collides with an atom by passing through the coulomb electric field of the nucleus and it will either interact with the nuclei of the atom or no interaction will take place. As

illustrated in Figure 2.1 [30], accelerated electrons interact with an atom differently. For instance, if an electron passes through the coulomb electric field without colliding with the nuclei, it will lose a small amount of its incident kinetic energy and release an x-ray of relatively low energy. Therefore the electron will collide into other atom or atoms in the target until it loses all its energy. On the other hand, if an electron happens to interacts with the nuclei of an atom inside the target, it will lose all its kinetic energy while generating an x-ray with the equivalent energy of the electron possessed before the incident.

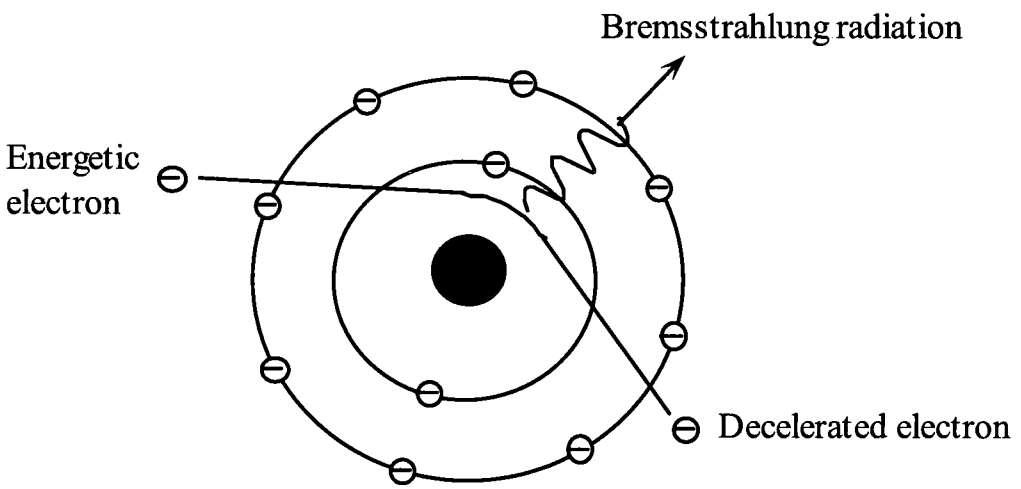

Figure 2.1 Schematic illustration of Bremsstrahlung radiation: an electron passing through the electric field of the target nuclei which creats Bremsstrahlung radiation and changes the electron original path [30].

2.2.3 Characteristic X-Rays

Instead of being generated by electrons interacting with the electric field of nuclei of the atoms as in Bremsstrahlung radiation, characteristic x-rays are generated from electrons transiting between atomic shells by creating a vacancy on the shell of the atom of the target metal. It means that the interactions happen between incident electrons and atomic electrons of the target.

Before going any further, a little basic knowledge should be reviewed here. According to the Bohr model of an atom, there are several shells on which the electrons are orbiting around the nucleus, and those electrons are bounded by different charges. The shells are named from the innermost one, which is called K shell and progresses in the order of the alphabet, such as L shell, M shell and so on, and so forth. The inner-most shell is occupied by two electrons that approximately contain the same amount energy (binding energy to the nucleus). On the next shell – L-shell, a maximum of 8 electrons are orbiting with approximately the same energy as well. However, they possess less binding energy than the ones which occupy K-shell.

Figure 2.2 [30] illustrates the characteristic x-ray production. An accelerated bombarding electron collides with a K-shell electron and after the electron obtains enough energy, it is liberated to the environment and leaves a vacancy on the K-shell. Therefore, a cascade of electronic transitions takes place inside the atom. The vacancy on the K-shell is refilled by another electron from another atomic shell, and then a vacancy is created on that shell which is again filled by another electron from a more distant outer shell. This continues till the electron from the environment fills the outermost shell. As mentioned before, electrons from each shell have well defined discrete energies, therefore,

when the electrons transit between the shells, energies are emitted in forms of photons, thus the characteristic x-rays are created. The characteristic x-rays are categorized according to which shells received the electrons and from where.

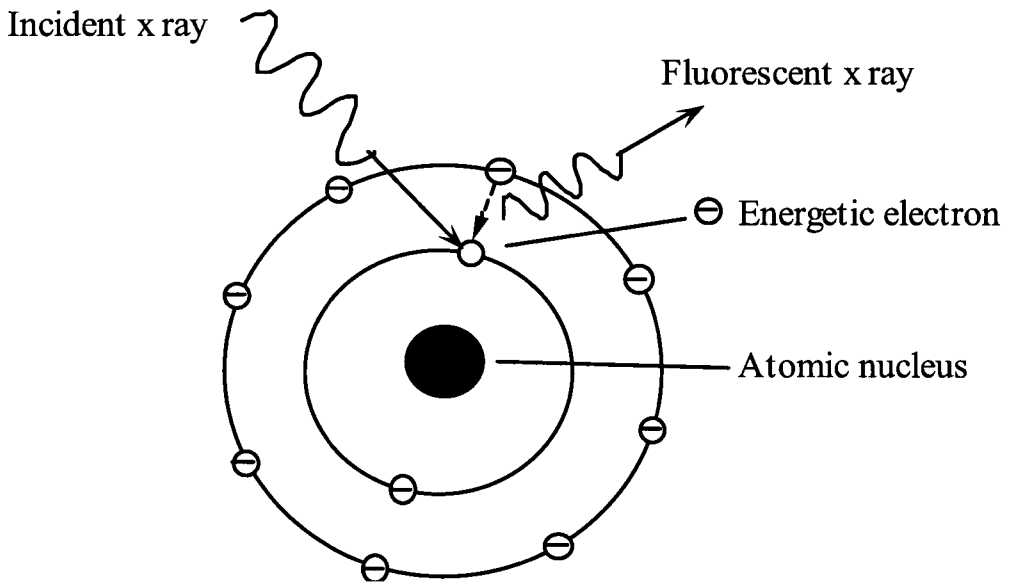

Figure 2.2 Schematic illustration of the creation of characteristic x-ray. Bombarding electron releases the electron on the innermost shell and leaves a vacancy behind. Characteristic x-ray is emitted, when an electron fills this vacancy from an outer shell [30].

For example, Figure 2.3 [30] illustrates the different energy levels of each shell and the emitted characteristic x-rays of Tungsten. As shown in the figure, the K-shell electrons of Tungsten are bonded with the energy of 70 keV, and the ones from the L-shell are bonded with the energy of 11 keV. In turn, when an electron fills the vacancy on the K-shell, it requires the emission of a 59 keV x-ray photon which is titled the K_α characteristic emission. If the vacancy on the K-shell is filled by an electron from the L-shell, the x-ray photon is carrying the energy of 67 keV, and it is named K_β characteristic

emission. Figure 2.3 shows the L_α characteristic emission and L_β characteristic emission as well, and the photon energies are 8 keV and 10.5 keV respectively.

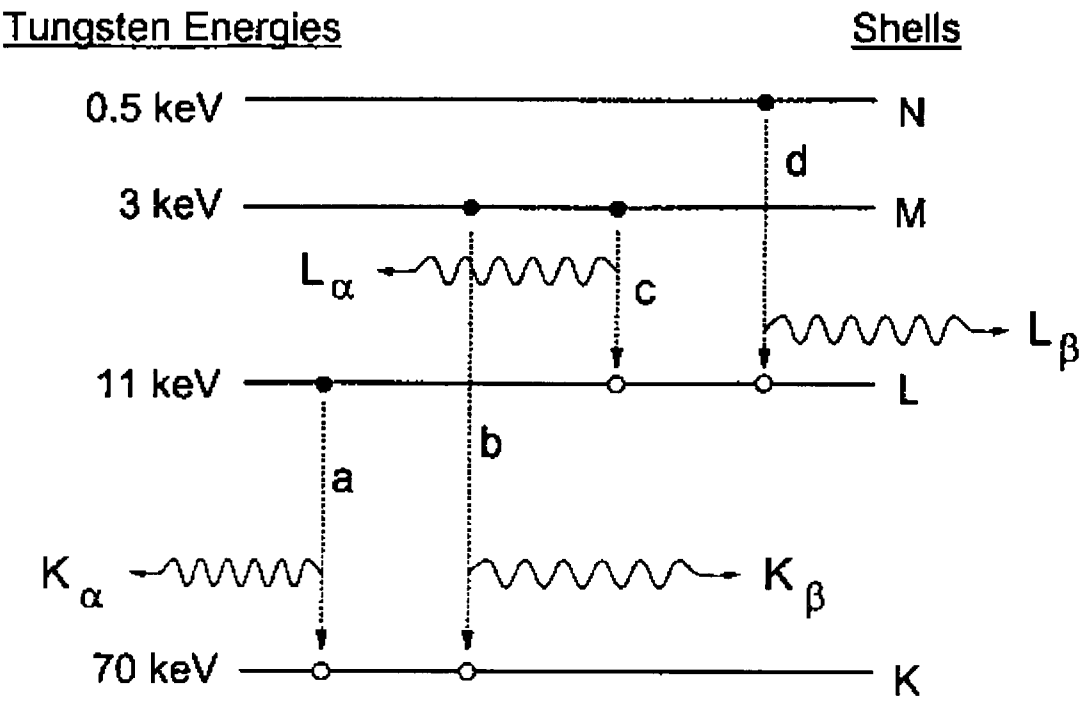

Figure 2.3 An energy diagram demonstrates the different energy levels of each shell and the emitted characteristic x-rays of Tungsten [30].

However, if the energy of bombarding electron is less than the binding energy of an electron of the atom of the target material, the orbiting electron will not obtain enough energy, thus the ejection of the electron will not occur.

2.3 X-ray Interactions

2.3.1 Introduction

X-ray photons interact with the object and pass their energy, and in some cases, the initial x-ray interactions will create x-rays in terms of scattered x-rays and characteristic x-rays. In this section, the interaction mechanism of Rayleigh scattering and Compton scattering are presented.

2.3.2 Rayleigh Scattering

Rayleigh scattering describes the phenomenon that the incident x-rays interact with the electric fields of orbiting atomic electrons without having ionization, and there is no energy exchange from the incident x-ray to the medium. The energy of the scattered x-ray is equivalent to the incident x-ray energy. As can be seen in Figure 2.4 [30], the incident x-ray carries the energy of E_0 which interacts with an atomic electron from the K-shell. However, instead of interacting with the electron itself, the interaction takes place between the incident x-ray and the electric field of the electron. Thus, there will be no energy exchange between the x-ray and the electron. The scattered x-ray shown in the diagram is E' where $E_0 = E'$, and it travels away from its original path with a certain degree of a scattered angle. Although energy exchanges do not exist in Rayleigh scattering, the x-ray experiences a change in its original path which will degrade the image resolution of the x-ray image detector systems. Consequently Rayleigh scattering is undesirable in medical imaging.

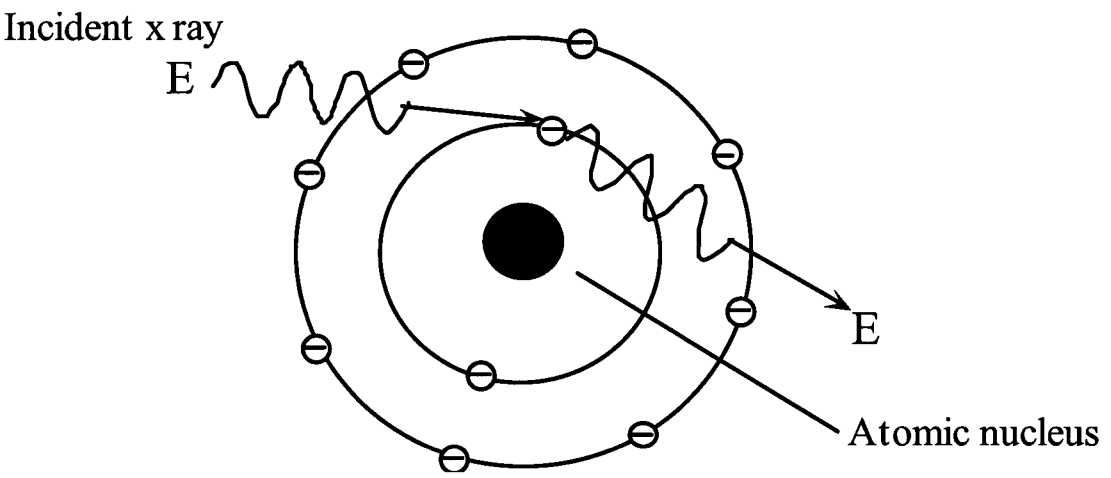

Figure 2.4 Schematic illustration of Rayleigh scattering: incident x-rays interact with the electric fields of orbiting atomic electrons without having ionization [30].

Typically, x-rays possessing higher energies have smaller scattering angles compared to the ones with lower energies, and Rayleigh scattering is more likely to occur in high-Z materials [30]. Figure 2.5 [30] shows the probability density function for Rayleigh scattering angles with different x-ray energies in water.

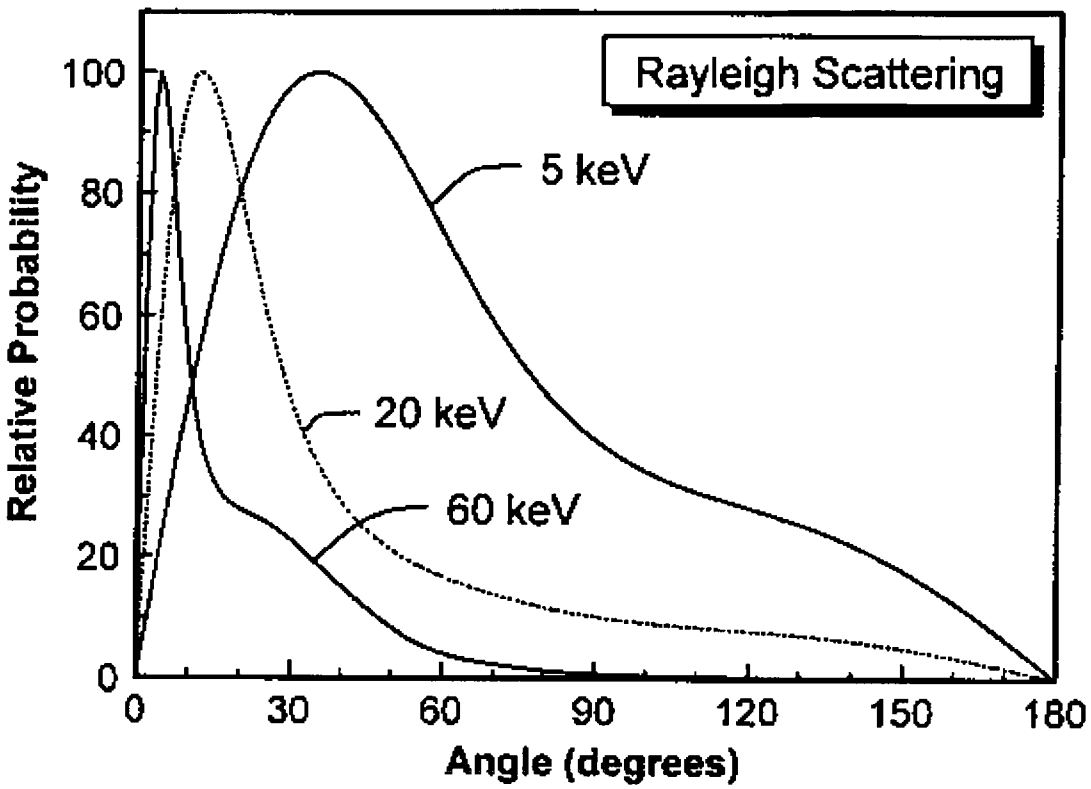

Figure 2.5 The graph demonstrates the probability density function of Rayleigh scattering angles with different x-ray energies in water [30].

2.3.3 Compton Scattering

Unlike Rayleigh scattering, Compton scattering involves ionization, and generally it occurs with higher energy x-rays. Typically, the interactions happen between incident x-ray and an outer-shell atomic electron.

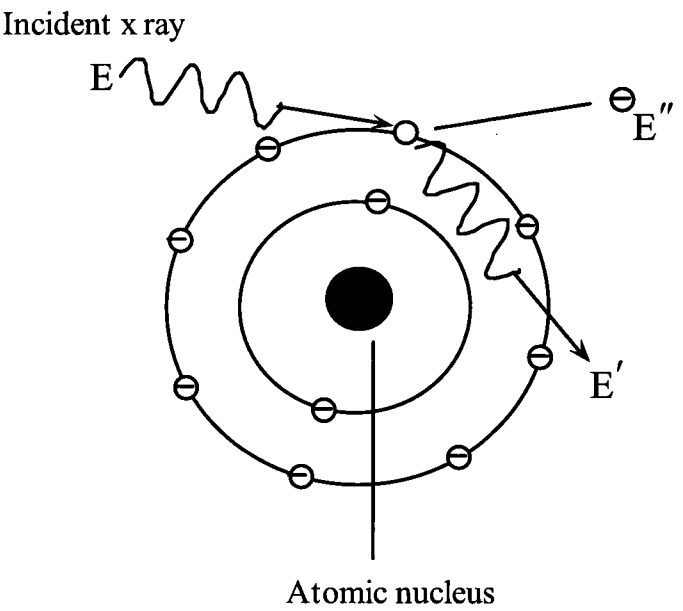

Figure 2.6 Schematic illustration of Compton scattering: incident x-rays interact with the orbiting atomic electrons and set them free, causing ionization; the path of the initial x-rays is changed [30].

As shown in Figure 2.6 [30], the incident x-ray carrying an energy of E_0 collides with an outer-shell atomic electron, and as a result, the electron obtains essential energy from the x-ray photon and is liberated from its parental atom with an energy of T. A scattered x-ray photon of energy E', and an ionized atom is left behind. Both the liberated electron and the x-ray photon travel away from where the initial interaction occurs. The scattering angle increases as the energy of the scattered x-ray photons becomes smaller [30]. Figure 2.7 [30] illustrates the probability density function for Compton scattering angles, and it is not hard to observe that the backscatters are preferable to the x-ray photons which have low energy.

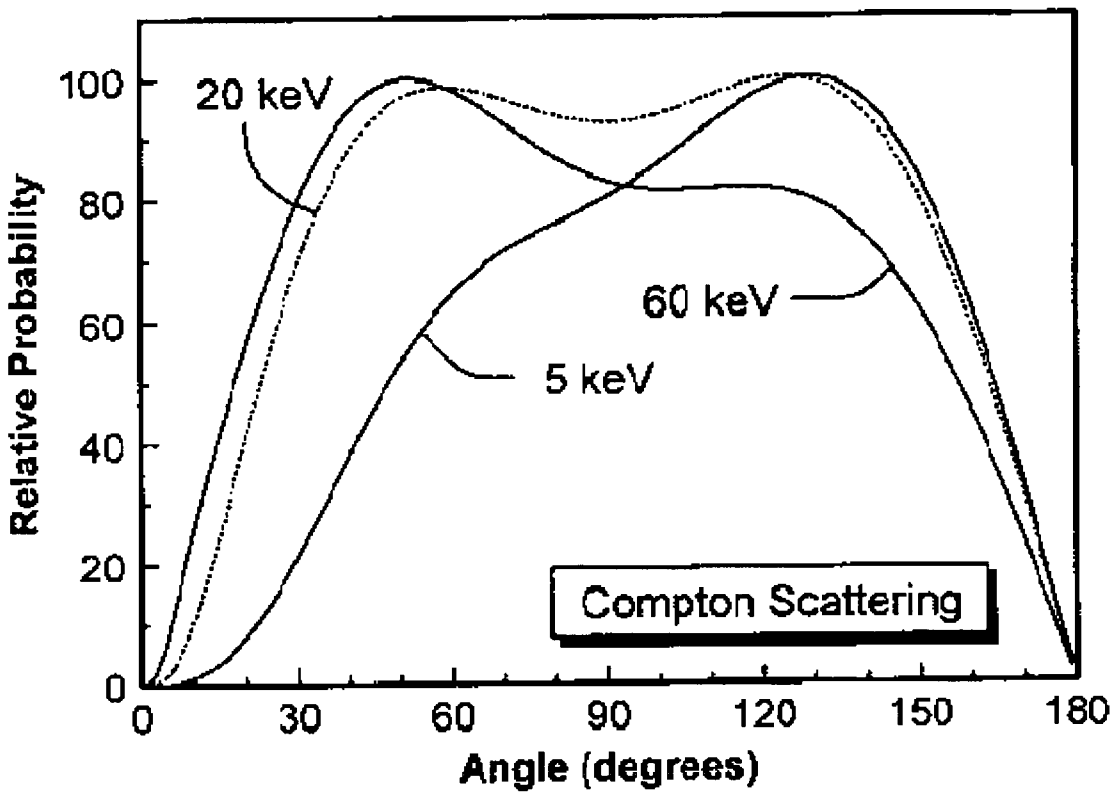

Figure 2.7 The graph demonstrates the probability density function for Compton scattering angles [30].

For diagnostic x-ray imaging (x-ray energy range from 10 keV to 100 keV), photon-photoconductor interaction is mainly photoelectric. Therefore, the generation of K-fluorescent x-rays is highly probable.

2.4 Ionization Energy

Ionization energy also known as ionization potential is the minimum energy required to eject an electron from its parental atom in order to create an electron-hole pair (EHP).

When the incident energetic particles or x-ray photons initially interact with the atoms inside the object, their energies are deposited to the atomic electrons and free them from their bound states of the parental atoms. Possessing the kinetic energy which is equivalent to the difference between the energy of the x-ray photon and the binding energy of the atomic electron, a primary photoelectron travels inside the object until it loses all its energy. Along its path, it causes more ionization and creates more EHPs.

For an x-ray image detector system, the ionization energy of the photoconductor is required to be as low as possible in order to generate as many EHPs as possible to increase the x-ray sensitivity. However, the dark current of the photoconductor is required to be negligible which implies that the photoconductor should have a wide band gap, which leads to a higher ionization energy and lower x-ray sensitivity. The ionization energy in a-Se depends on the electric field and it decreases as electrical field increases [31]. For amorphous-Selenium (a-Se) at the electric field of 10 V/um, the required ionization energy is about 45 eV; whereas for polycrystalline materials like poly-HgI_2, and polycrystalline Cadmium Zinc Telluride (poly-CdZnTe) it is typically around 5 eV [30].

2.5 X-ray Imaging Detector Materials

2.5.1 Introduction

In an x-ray image detector system, the photoconductor is the core, and the design and properties of the photoconductor affect the performance of the flat-panel detectors. In Section 1.6, the ideals of a photoconductor were discussed. This section will review a few material structures and discuss one of the most common materials which are currently used for flat-panel x-ray image detectors. Important properties of the material are discussed and compared with the ideal case.

So far, stabilized a-Se is the best choice of photoconductors for diagnostic purposes. However, other materials such as poly-HgI_2, CZT and PbO are very competitive materials for photoconductors as well.

2.5.2 Polycrystalline and Amorphous Solids

A perfect elemental crystal consists of periodically arranged atoms which have identical distances and angles to their adjacent atoms, and there are a strict number of bonds to its immediate neighbors. Thus a perfect elemental crystal has a periodic structure and maintains a long-range order.

Polycrystalline solids' structure is different from perfect elemental crystal. Instead of having one whole single crystal, it is composed of many crystallites which are disoriented and placed randomly. Those crystallites are called grains, and between each grain, there are grain boundaries, as shown in Figure 2.8 [32]. The atoms which exist in the grain boundaries have broken or extended bonds, and some of them are misplaced and cannot have the same crystalline pattern as either of the surrounding grains. In general, impurities in a polycrystalline solid exist where the grain boundaries are.

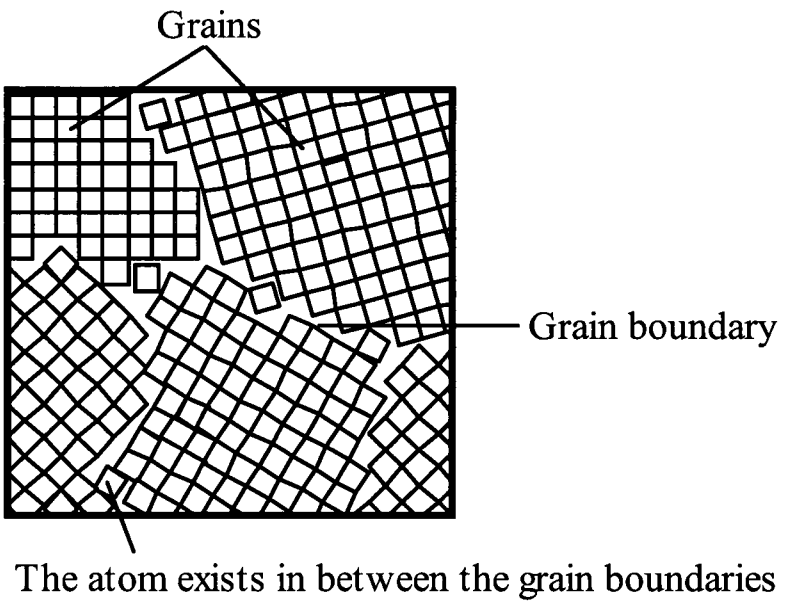

Figure 2.8 The graph demonstrates the structure of a polycrystalline solid [32].

Amorphous solids do not possess long-range order of the positions of the atoms, and instead, short-range order commonly exists in amorphous solids. Atoms in amorphous solids do not have identical distances and angles to each other, and the number of immediate bonds varies for different atoms. Lacking long-range order, amorphous materials have many advantages which make it possible for them to be applied to certain objects, such as thin films.

2.5.3 Amorphous Selenium

Selenium is an element which exists in the VI group of the periodic table, and it belongs to a group of elements called chalcogens. The atomic number of Selenium is 34, and in total, one selenium atom has 28 inner core electrons and another six electrons on its valance band.

Amorphous-Selenium (a-Se) and its alloys have been well studied due to their photo-conducting properties. The density of a-Se is 4.5 gm/cm^3, relative permittivity is 6.7 and the energy gap is 2.22 eV. Currently, a stabilized a-Se photoconductor is one of the most preferred photoconductors used for large-area flat-panel x-ray imaging detectors for diagnostic purposes. The reason for this is, a stabilized a-Se can be easily deposited as an uniform thin film quickly to a large area, such as 40X40cm, and a stabilized a-Se is commonly alloyed with 0.3% Arsenic (As) atoms and doped with ppm-level Chlorine. Another advantage of a-Se is that it can be coated by conventional vacuum deposit to form a thick film without raising the temperature of the substrate above 70 °C. By contrast, neither pure nor crystalline Se is suitable for x-ray photoconductors since pure a-Se is thermally unstable and crystallizes over time. Also, the dark current resistivity of crystalline Se is much lower compared to a-Se, so it will end up with a large magnitude dark current that will degrade the x-ray image quality. In general, a-Se is alloyed with As with a range from 0.2% to 0.5% to improve the stability and prevent crystallization, but As impurity will create deep trap hole. Thus, the solution is doped in the alloy with 10-20 parts per million (ppm) of a halogen, for example Chlorine which will eliminate the side effect of As impurity by restoring the hole life time to its initial value. The a-Se alloyed with 0.2%-5% As and ppm-level Cl is called stabilized a-Se.

There are two kinds of traps in a-Se: shallow and deep traps. Shallow traps are usually distributed near the band edges, and reduce the drift mobility of the carriers. The extended state mobility μ_0 (at room temperature for hole: ~0.3 cm^2/V-s; for electron: ~0.1 cm^2/V-s) [33] [34] of the carriers in the extended states is reduced by the shallow trap

(trapping and release), so the actual carriers' mobility is effective mobility μ, which is given by [6]:

$$\mu = \frac{\tau_c}{\tau_c+\tau_r}\mu_0, \qquad (2.1)$$

where, τ_c is the average capture time of a shallow trap center. It is the time before a drifting mobile carrier in the extended states is captured by a shallow trap center; τ_r is the time a carrier remains trapped in a trap center before it is released, which is called the release time. Generally, the release time of a shallow trap is very short and a carrier being drifting across the detector might experience many shallow trap capture and release events. At room temperature, the effective hole mobility μ_h is ~0.12 cm^2/V-s, and effective electron mobility μ_e is 0.003-0.006 cm^2/V-s.

After being captured by a shallow trap center, a carrier is released after a certain period, but if a carrier is trapped by a deep trap center, it is permanently removed from conduction, since the deep trapping time of deep trap is relatively long. Therefore, the carrier life-time depends on deep traps rather than shallow traps, and it varies from sample to sample due to the difference of the impurities and the preparation of the materials. In a-Se material, an electron's lifetime is sensitive particularly to impurities: increasing the doping concentration of As will increase the electron's lifetime, and by contrast, increasing Cl doping concentration will decrease it. On the other hand, hole lifetime depends more on the substrate temperature, as it decreases dramatically if the temperature of the substrate drops. Increasing As and Cl doping concentration will decrease and increase the hole lifetime respectively [35]. In stabilized a-Se materials, the typical hole lifetime is 10-500 μs, and 100-1500 μs for electron [36]. Adjusting the doping concentration of As and Cl will help control electron and hole lifetimes. Carrier

trappings have a significant effect on the imaging properties of the detectors, such as sensitivity and resolution.

2.6 X-Ray

2.6.1 X-Ray Filtration

Generally, x-ray spectra applied for diagnostic radiology are generated by an x-ray tube with Tungsten, Molybdenum or Rhodium as target material, and the kVp range varies from 40 kVp ~ 150 kVp for Tungsten; 4 kVp ~ 35 kVp for molybdenum and Rhodium. The x-ray spectra vary with the same x-ray generating system because of the calibration and generator waveform of different x-ray systems and the amount of filtration [30]. Generally, filtrations are applied before x-rays reach the objects, since filtration has a profound effect on the x-ray beam quality [37]. Without added filtrations, the low-energy x-rays from the tube will be absorbed by the patients and unlike high-energy x-rays, they will not be able to penetrate the patient and reach the x-ray detector. Thus, low-energy x-rays will not contribute to the image result. Consequently, additional filtrations are useful to reduce or even eliminate the low-energy x-rays in order to reduce the radiation dose to the patients [38]. Figure 2.9 [30] illustrates the differences of x-ray spectrum, with and without additional filtrations.

For an x-ray generating system, the filtration consists of two parts: inherent filtration and added filtration. Inherent filtration refers to the filtration that occurs in the x-ray beam path as a part of the x-ray tube, which usually includes a layer of glass or metal, a thin layer of oil, a plastic x-ray tube port, and in some cases a mirror [30]. Added filtration, apparently is the extra filtration from the inherent filtration, and mostly is a

sheet or several sheets of metal (such as, Aluminum, Copper etc.) and they are added in the beam path. Therefore, the total filtration for an x-ray generating system is the sum of the inherent and added filtration.

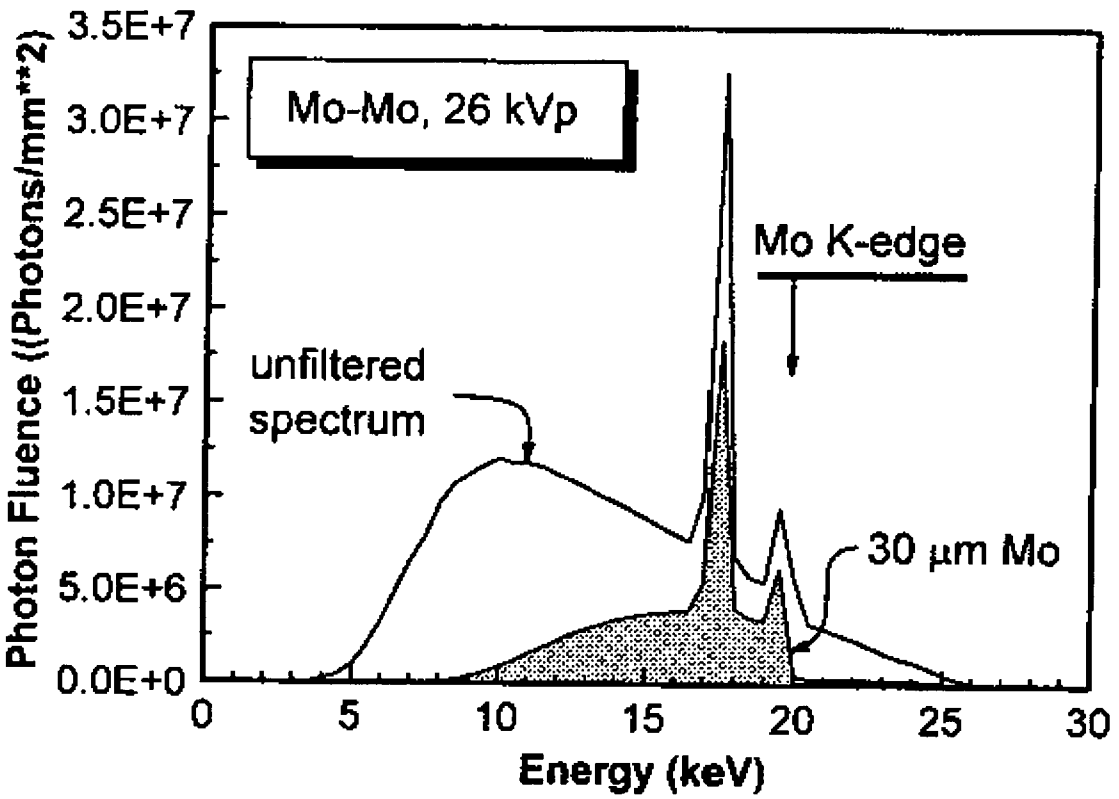

Figure 2.9 A molybdenum x-ray spectrum produced at 26 kVp is demonstrated with and without added filtrations: shaded area is the x-ray spectrum with 30 um Mo filter [30].

2.6.2 Average and Effective Energy

Average and effective energy are the terms used to describe an x-ray spectrum. Average energy of an x-ray spectrum is the weighted energy of the spectrum:

$$E_{ave} = \frac{\int_{E_{min}}^{E_{max}} \Psi(E)dE}{\int_{E_{min}}^{E_{max}} \Phi(E)dE}, \quad (2.2)$$

where E is the energy of x-ray spectrum, $\Phi(E)$ is the photon fluency (photons/mm^2) corresponding to energy E, and $\Psi(E)$ is the corresponding energy fluency (joules/mm^2), and

$$\Psi(E) = \Phi(E) \times E. \quad (2.3)$$

Effective energy estimates the penetration power of the x-ray beam, and it is typically estimated when only the attenuation data is available, and it can be assessed by using the monoenergetic Labert-Beers equation [30]:

$$\frac{N}{N_0} = \exp(-\mu x), \quad (2.4)$$

where, $\frac{N}{N_0}$ can be measured, μ is the linear attenuation coefficient, and x is the thickness of the detector. By plotting and comparing the log-log graphs, the effective energy is evaluated.

2.7 Modulation Transfer Function

Resolution is a useful parameter to describe the ability of a system to distinguish two distinct objects which are placed closely together, and the minimum distance with which the system can distinguish the objects is called "resolution". However, the

resolution sometimes also depends on the shape of the objects, and delta function is used to test the response of the system. This response is called point spread function (PSF). The term modulation transfer function (MTF) is commonly used to describe the resolution of an x-ray image system by engineers and scientists. The MTF is the relative response of the system as a function of spatial frequency.

MTF is the absolute value of two-dimensional Fourier Transform as a function of spatial frequency of PSF. It is a useful method to evaluate the performance of an x-ray image system. An imaging system can be described as a cascade of many elementary stages. The composite MTF of a system is simply the product of the MTF of all individual stages. The response along a line perpendicular to the spatial axis of a system to a "line" delta function can be described by Line Spread Function (LSP), normalized to unity area. It is impossible to measure two-dimensional MTF, so practically one-dimensional MTF is used which is the one-dimensional Fourier Transform of LSP. The MTFs of an amorphous-Selenium based direct-conversion flat-panel x-ray imaging detector system can be evaluated individually.

2.7.1 MTF Due to Primary Photoelectric Effect

Photoelectric effect discovered by Heinrich Rudolf Hertz is a phenomenon where electrons are emitted from matter when they absorb the energy carried by x-ray photons or other radiations.

After being generated from the x-ray tube, first, x-ray photons will interact with the object, which is placed in between the x-ray tube and the photoconductor. X-rays interact with tissues that are mainly consisted of hydrogen, carbon, nitrogen and oxygen. All of these elements have low K-shell binding energy, so the character x-rays generated

by the interaction of the incident x-ray photons and these elements will not travel far, mostly within the adjacent tissues. Because tissues have different "radiodensity" (attenuation), they will absorb x-rays differently. Due to this difference, the images collected at the terminal (e.g. monitor) appear differently.

After the interaction with the object, x-rays arrive at the surface of the detector with a different profile due to the attenuation contrast of the object. When x-rays penetrate into the photoconductor layer, a fraction of the x-rays are absorbed in the layer, and the absorption (attenuation) is strongly energy dependent [25]. X-ray photons interact with the a-Se atom and create free electron-hole pairs on their pass if the energy of x-ray is higher than the binding energy of the Se electron. However, if the energy is less than the binding energy, the electrons will not obtain enough energy to be emitted from the atom, or at least the inner most shell – K-shell will not release electrons, since the electrons on this obit have the greatest binding energy. The electrons on the outer shell, such as L-shell, M-shell, which have less binding energy might be set free when they absorb the energy from the photons. When the incoming x-ray energy is higher than the binding energy, a chain reaction is likely to take place. This is the photoelectric effect.

First, the x-ray photons are carrying a certain amount of energy, and when they interact with the Se atom, most probably the electrons from the inner most shell – K-shell will be released from the state that they are bounded to. Before an electron is liberated from its parent atom it has to first overcome the binding energy. Carrying the kinetic energy they then travel away from the parental atoms, which was discovered by Einstein in 1905. The relationship of the x-ray energy E_0, binding energy E_B, and the primary photoelectron's kinetic energy E_k is:

$$E_k = E_0 - E_B \quad [2.5]$$

After the primary photoelectron is ejected from the parent atom, a vacancy exits in the K-shell, and electrons from the outer-shell will fill the vacant shell, until all the vacancies are filled, and vacancy exists at the outermost shell will be filled by a free electron from the medium. During this transition, when the outer-shell electron jumps to the inner shell, the energy will be released in the form of x-ray photons. Thus a primary photoelectron collides with other Se atoms and releases more secondary electrons, until it loses all its kinetic energy; and the secondary electrons will release more electrons if they have enough energy, and so on.

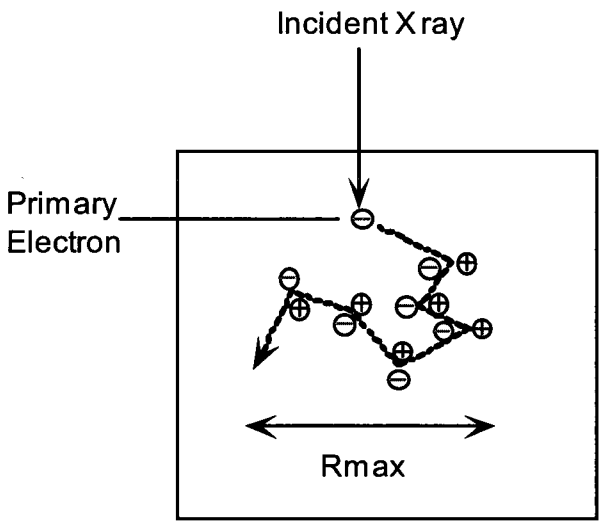

Figure 2.10 The mechanism of signal spreading due to primary photoelectric effect.

By the end of the primary photoelectric effect, a sphere-shaped cloud of electrons and holes are created, and the size of the sphere determines the spatial resolution of the detector, as illustrated in Figure 2.10. The spatial resolution is a function of the range of

the primary photoelectron, and Que and Rowlands [25] calculated the MTF due to primary photoelectric effect by using an analytical model based on the assumption that when the incoming x-rays energy is higher than the K edge (Se: 12.658 kev), the primary photoelectron is ejected from the K-shell. The MTF due to the range of primary photoelectric effect is given by [25]:

$$MTF_{pe} = \exp(-\pi^2\sigma^2 v^2) \tag{2.6}$$

where v is the special frequency; σ is a parameter proportional to the maximum path length R_{max} of the primary electron travels. Kanaya and Okayama [39] have given an expression for R_{max} in millimeter at the energy range 10-1000 keV [39]:

$$R_{max} = 2.76 \times 10^{-5} \times \frac{M_a E^{5/3}}{\rho Z^{8/9}} \tag{2.7}$$

where M_a is the atomic mass (g/mol), E is the primary photoelectron's energy (keV), ρ is the density (g/cm^3), and Z is the atomic number. According to Que and Rowlands' estimation, the relation is: $\sigma \approx R_{max}/2.5$ [25]. Notice that, Euqation 3.2 calculates MTF_{pe} based on the assumption that the maximum intensity of the charge carriers is located in the center of the sphere-shaped cloud, and the charge carriers are distributed according to Gaussian form.

2.7.2 Trapping Related MTF

2.7.2.1 Introduction

After electron-hole pairs (EHP) have been generated by the incoming x-ray photons during the primary photoelectric interaction and secondary interactions, they are drifted by the electric field added in between the top and bottom electrodes. When the

carries are drifted across the bulk of the photoconductor, they might be captured by the trap centers, and some of them are captured by deep traps where they will not be released during the time scale of observation. If a carrier is trapped on its way to the electrode, it not only reduces the charge collected on the corresponding pixel, it also induces the charge on the neighboring pixels. Consequently, the spatial resolution of the imaging system is degraded.

Kabir and Kasap [26] have given an analytical expression for calculating the modulation transfer function due to the carriers trapped (MTF_{trap}) in the bulk of the photoconductor of a direct conversion flat panel x-ray image detector.

2.7.2.2 MTF_{trap}

We can assume that a direct-conversion flat-panel x-ray imaging detector's lateral dimension is much greater than the thickness (L) of the detector. A photoconductor is sandwiched between two electrodes: the top electrode –where the x-ray initially arrives and the bottom electrode – where the pixels are placed. Each pixel is connected to an amplifier which collects the information (charges) from the pixel during the integration time. As shown in Figure 2.11 [36], a sketch of a direct-conversion flat-panel x-ray detector, the top electrode is negative biased. Consequently an electric field (F) is established in the photoconductor. We assume the electric field is uniform, and the carriers are drifted following the field lines towards the bottom electrode in the photoconductor. When the carriers are generated inside the photoconductor by the x-ray, they are drifted by the electric field along the electric field lines across the

photoconductor, and the diffusion here has been neglected because of the high electric field.

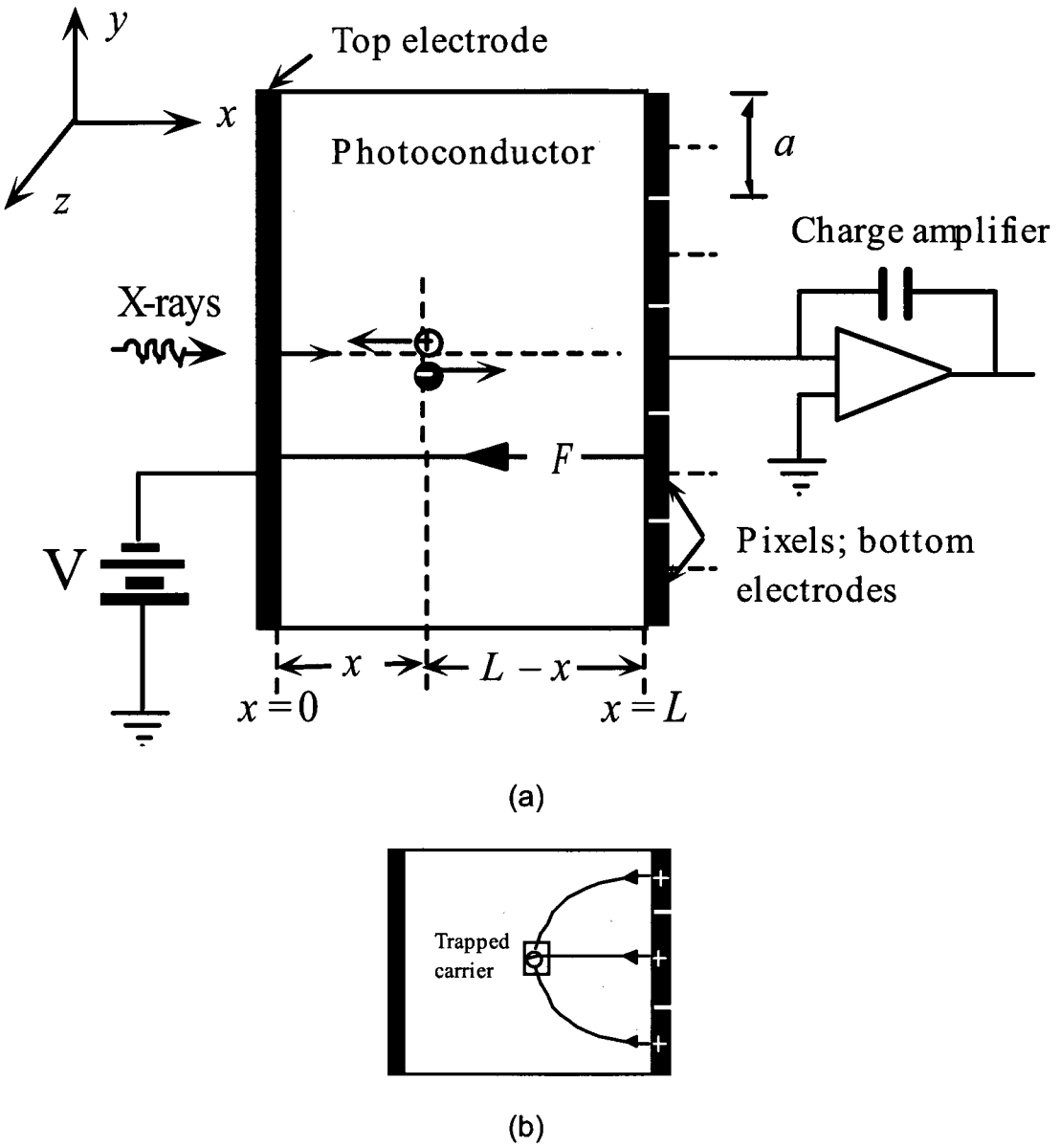

Figure 2.11 (a) A Schematic illustration of a direct-conversion flat-panel x-ray imaging detector with top electrode negatively biased. (b) Trapped charge carriers reduce the imaging information on the centre pixel and reduce signal on the surrounding pixel electrodes, and spread the information which leads to the resolution deduction [36].

If c'_t and c'_b are the carrier concentration of the charge carriers drifted towards the top and bottom electrodes respectively, and B is the carrier concentration at $x' = 0$ and $t' = 0$, then the initial carrier concentration across the photoconductor for a short x-ray pulse yields [26]:

$$c'_t = c'_b = B \exp(-\mu x'), \qquad (2.8)$$

where α is the linear attenuation coefficient of the photoconductor. To simplify the calculation, c' is normalized to:

$$c = c'/c_0, \qquad (2.9)$$

and c_0 is given [26]:

$$c_0 = \frac{1}{L}\int_0^L B\, e^{-\mu x} dx = B\Delta(1 - e^{-1/\Delta}), \qquad (2.10)$$

where $x = x'/L$, $y = y'/L$ and $z = z'/L$, and normalized attenuation depth is $\Delta = 1/\mu L$.

2.7.2.3 MTF_{trap}

The Line Spread Function (LSP) due to charge carrier trapping is given by Kabir and Kasap [26]:

$$L = \frac{1}{2\pi}\int_{-\infty}^{\infty}\int_0^1 \sum_{k=-\infty}^{\infty} \frac{q_t(x)(1-x+2k)}{[(1-x+2k)^2+y^2+z^2]^{3/2}} dxdz + Q_b\delta(y), \quad (2.11)$$

Where, k is an integer and Q_b is the normalized mean number of carriers that reach the bottom electrode [26]:

$$Q_b = \frac{\tau_b(\exp(-1/\Delta) - \exp(-1/\tau_b))}{\eta\Delta(1-\tau_b/\Delta)}, \qquad (2.12)$$

where,

$$\tau_b = \frac{\mu\tau'_b F}{L}, \tag{2.13}$$

and,

$$\eta = (1 - \exp(-1/\Delta)). \tag{2.14}$$

The Fourier Transform to L is given by [26]:

$$G(f) = \frac{(\tau_b+\tau_t)(\omega\text{cosech}\omega-\exp(-1/\Delta)\omega\coth\omega-\Delta^{-1}\exp(-1/\Delta))}{\eta\Delta^2(1-\tau_b/\Delta)(1-\tau_t/\Delta)(\Delta^{-2}-\omega^2)}$$

$$- \frac{(\omega\text{cosech}\omega-\exp(-1/\tau_b)\omega\coth\omega-\tau_b{}^{-1}\exp(-1/\tau_b))}{\eta\Delta(1-\tau_b/\Delta)(1-\tau_t/\Delta)(\tau_b{}^{-2}-\omega^2)}$$

$$+ \frac{(\exp(-1/\Delta-1/\tau_t)\omega\text{cosech}\omega-\exp(-1/\Delta)\omega\coth\omega-\tau_t{}^{-1}\exp(-1/\Delta))}{\eta\Delta(1+\tau_t/\Delta)(\tau_t{}^{-2}-\omega^2)}$$

$$+ \frac{\tau_b(\exp(-1/\Delta)-\exp(1/\tau_b))}{\eta\Delta(1-\tau_b/\Delta)}, \tag{2.15}$$

where, f is the normalized spatial frequency: $f = f'L$ (f' is the actual spatial frequency), $\omega = 2\pi f$, τ_t is the normalized life time of the carrier moving towards the top electrode and τ_b is the one towards the bottom electrode [40]:

$$\tau_t = \frac{\mu\tau'_t F}{L}. \tag{2.16}$$

When f=0, the expression for G(0) is given by [26]:

$$G(0) = \frac{(\tau_b+\tau_t)(1-\exp(-1/\Delta)-\Delta^{-1}\exp(-1/\Delta))}{\eta(1-\tau_b/\Delta)(1-\tau_t/\Delta)}$$

$$- \frac{\tau_b(\tau_b-\exp(-1/\tau_b)-\tau_b\exp(-1/\tau_b))}{\eta\Delta(1-\tau_b/\Delta)}$$

$$+ \frac{\tau_t(\tau_t\exp(-1/\Delta-1/\tau_t)-\exp(-1/\Delta)-\tau_t\exp(-1/\Delta))}{\eta\Delta(1+\tau_t/\Delta)}$$

$$+ \frac{\tau_b(\exp(-1/\Delta)-\exp(1/\tau_b))}{\eta\Delta(1-\tau_b/\Delta)}. \qquad (2.17)$$

The MTF is conventionally unified at zero frequency. Therefore, the Modulation Transfer Function due to bulk trapping can be expressed:

$$MTF_{trap}(f) = \frac{G(f)}{G(0)}. \qquad (2.18)$$

2.7.3 Aperture MTF

Modulation Transfer Function due to aperture is associated with the aperture function of the pixel electrodes of the detector, and MTF_{ap} is considering the average signal over the area of pixel apertures. It can be used to evaluate part of the spatial resolution of an x-ray image detector system by describing how special frequencies pass through the apertures of the detector.

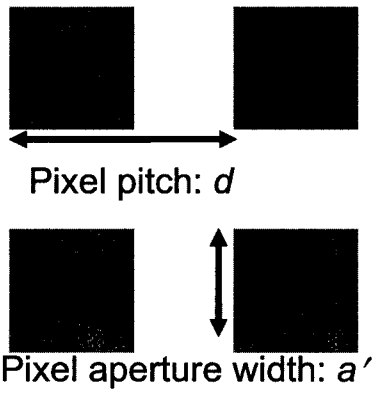

Figure 2.12 A sketch of pixel apertures of a imaging detector system.

Figure 2.12 [41] depicts a sketch of pixel apertures. It assumes that the detector apertures consist of many small squares with a dimension of α. this distance is called pixel width, which is usually smaller than the width of pixel pitch. The effective pixel aperture is approximately equal to the pixel pitch. Therefore, the MTF_{ap} is given by [27]:

$$MTF_{ap}(f) = |\mathrm{sinc}(\alpha f)| = |\frac{\sin\pi\alpha f}{\pi\alpha f}|. \qquad (2.19)$$

The highest frequency can be scanned by an x-ray image detector system depends on the pixel pitch d, and the highest frequency that can be scanned is $1/2d$ [41].

2.7.4 MTF for the Reabsorption of K-Fluorescent X-Ray

After a primary photoelectron is emitted from its parental atom, within the atom there will be a cascade of electron transitions. This leads to the creation of fluorescent x-rays. These x-rays are then absorbed at different points from where the primary x-ray

interacts. This process degrades the image quality. Detail analysis and discussions will be presented in Chapter 3.

2.8 Summary

The important concepts related to x-ray detectors are reviewed in this chapter. This thesis concentrates on a-Se based direct-conversion flat-panel x-ray imaging detectors and their MTFs. In next chapter, the details of MTF due to the reabsorption of K-fluorescent x-ray and overall MTF model will be presented.

Chapter 3 Modulation Transfer Function

3.1Introduction

Modulation/Resolution Transfer Function (MTF) is a useful model to evaluate an x-ray imaging detector system, and studying the inherent spatial resolution will help assess the performance of an x-ray imaging detector system and determine the facts that affect the quality of the x-ray images. Typically, the spatial resolution is described in terms of MTF.

Many effects have been made to discover the causes of degradation of the spatial resolution of direct-conversion flat-panel x-ray imaging detector systems [25] [26]. Based on current understanding, reabsorption of K-fluorescent x-ray photons, the range of primary photoelectrons, charge carrier trapping and aperture are the dominant mechanisms responsible for the loss of resolution in direct-conversion flat-panel x-ray imaging detectors. A model is proposed in this thesis to evaluate the overall MTF of the detector considering all the mechanisms mentioned above.

3.2 Overall MTF Model

The total MTF is the product of the MTFs of all the independent stages. There are three scattering stages:

(1) Scattering of x-ray photons before electron-hole pairs (EHPs) creation (this stage includes the effect of primary photoelectron and the reabsorption of K-fluorescent photons);

(2) Blurring due to the carrier trapping;

(3) Aperture blurring.

In the first stage, MTFs due to the primary photoelectron and the reabsorption of the K-fluorescent x-rays are additive with weighting factors according to the projection probabilities. The dominant secondary photons that are absorbed inside the photoconductor are K-fluorescent photons. [42,43,44]

All the MTFs are normalized to 1 at zero spatial frequency. The MTF due to all the effects is denoted as MTF_{total}, which is weighted MTF:

$$MTF_{total} = (\rho_{pe} MTF_{pe} + \rho_k MTF_k) \times MTF_{tr} \times MTF_{ap} , \qquad (3.1)$$

where, ρ_{pe} is the fraction of photoelectric attenuation that contributes to the primary photoelectric effect, and ρ_k is the fraction of photoelectric attenuation that contributes to the reabsorption of K-fluorescent x-rays. The details and the calculation of ρ_k is presented in Chapter 3.3.3. The relationship between ρ_{pe} and ρ_k is:

$$\rho_{pe} = 1 - \rho_k . \qquad (3.2)$$

3.3 Modulation Transfer Function for the K-fluorescence

Photoelectric interaction creates electron-hole pairs (EHP) by absorbing the energy from incoming x-ray photons inside the photoconductor, and carrying a certain amount of energy these EHPs travel away from the initial interaction site. After the electrons are liberated from their parental atom, there is a cascade of electronic transitions inside the atoms. This series of transitions create photons which are known as K-fluorescent x-ray within the photoconductor, and they travel away from the initial spot

where they were generated. While traveling away from the initial spot, they create more EHPs which will degrade the spatial resolution.

A photoconductor of an amorphous-Selenium based direct-conversion flat-panel x-ray imaging detector can be viewed as a space filled with Selenium atoms where the electrons orbit around them. Incoming x-rays are absorbed when they first interact with the detector, as has been discussed in section 2.7 in terms of photoelectric event. Within each atom, there are two electrons orbiting on the innermost electronic shell - K shell where the electrons have almost the same amount of binding energy. Outside of the K shell is the L shell which is occupied by 8 other electrons carrying a binding energy which is much smaller than the energy possessed by the K-shell electrons. The ordering of the electron shells starts from K and then increases alphabetically. During the initial absorption of the incoming x-ray, a vacancy is created on K shell or L shell, which depends on the energy of the incoming x-ray. As it has been discussed before, when the incoming photon energy is higher than the K shell binding energy, the K-shell electron will obtain energy from the photon and will be liberated from its parent atom. A cascade of electron transition will then occur in the atom. The empty spot left on the K shell will be filled by other electrons from the outer shell, and result in creating another vacancy on this shell. This will keep going on until the outmost shell's vacancy is filled by the electrons from the environment, where many free electrons have been created by photoelectric effect and this electronic transition process.

During this cascade electron transition process the vacancies created are filled by the electrons from the outer shells energy which are emitted because of the different energy levels possessed by the electrons on different shells. The energy levels of each

shell are well defined at discrete quantized values, so this energy emission is required when one outer shell electron jumps to an inter shell, and the amount of energy emitted is certain. The energy is emitted in the form of photons, and there are different photon emissions. K_α and K_β emissions mean K shell is the receiving shell of the transition; α means the electron is coming from the next shell up, for example for K_α emission, the electron that fills in the vacancy on the K shell comes from L shell; β emission means the transmitted electron is from two or more shells away, for instance, shell M or N are two or three shells away from K shell.

K_α and K_β emission together are titled as K-fluorescent x-ray and they will travel from the place where the x-ray initially interacted, until it is reabsorbed inside the detector. This reabsorption of K-fluorescent x-ray away from the initial interactional spot degrades the resolution of the imaging detector system.

In amorphous-selenium, the energies E_α and E_β of K_α and K_β are 11.2 keV and 12.5 keV respectively, W. Que and J. A. Rowlands have proposed a numerical MTF model due to the effect of the reabsorption of the K-fluorescence. The model is based on calculating the point spread function (PSF) of the detector and subsequent two-dimensional Fourier transform of the PSF. In this thesis, we propose a simplified analytical model to evaluate the MTF due to K-fluorescent x-ray reabsorption by determining the Line Spread Function (LSF) and subsequent one-dimensional Fourier transform.

As it shown in Figure 3.1, the K photons are created within a small area inside the detector, where we assume that the detector is a plain sheet of infinite extent. We are using K photons here, since the only difference between K_α and K_β photons is the

energies they are carrying, they can be combined together and be called K photons. The energy E_k = 11.375, is given by E. Storm and H. I. Israel [45].

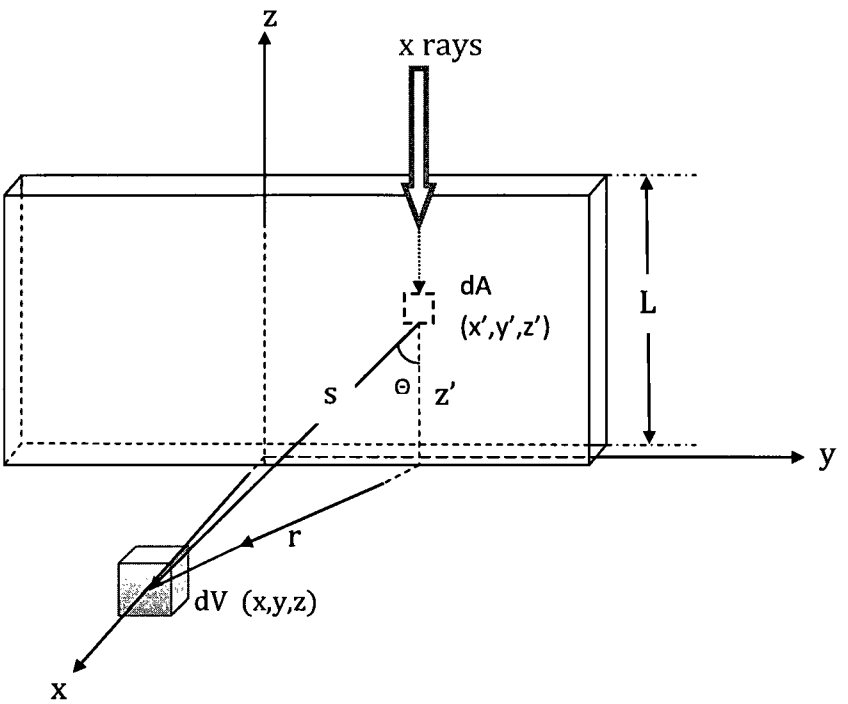

Figure 3.1 MTF model of the K-fluorescent x-ray absorption.

The K photons travel away from the initial interaction site (dA in Figure 3.1) until they are reabsorbed within the detector as discussed. The photons can be emitted to any direction in the detector and we can imagine that all the photons are travelling within a sphere, and there is a possibility that the photons could be absorbed at any point within the sphere.

X-rays are shinning on the detector along the yz plane at x=0. The Line Spread Function (LSP) is calculated by finding the number of K-fluorescent x-rays from the

emitting element dy'dz'(a small area inside the yz x-ray interaction plane) that pass through the volume of a small cube dV along the x-axis. This is then divided by dA and integrated over y from -∞ to +∞ and over z from 0 to L. The solid angle subtended by dA, is $dA \cdot cos\theta/4\pi s^2$. Along the path a K photon travels, it attenuates exponentially – exp $(-\mu_k \cdot s)$, where μ_k is the attenuation coefficient of K photons.

It has been considered that when the initial x-ray photons arrive at the photoconductor, they interact with the atoms along the yz plane at x=0 and attenuate exponentially on their way passing through the photoconductor: exp $(-\mu(L-z))$. As shown in Figure 3.3, L is the thickness of the detector and z is the distance from where the x-ray photons are initially interacted with the bottom electrode of the detector, so L represents the distance x-ray travels inside the detector before it interacts with the selenium atom. As it has been discussed before, K photons are emitted where the initial interaction happens, and travel within the detector. We assume a K-fluorescent x-ray photon is traveling from the shaded area dy'dz' to the shaded cube dV along s - the distance a K photon travels. Along the path a K photon travels, it attenuates exponentially: exp($-\mu_k \cdot s$), where μ_k is attenuation coefficient of K photons. Here we assume x-rays travel from z = +∞ to the negative z direction and interact at the yz plane. The Line Spread Function (LSF) is calculated by finding the number of K-fluorescent x-rays from the emitting element dy'dz', that pass through the volume of a small cube along the x-axis and is then divided by dA and integrated over y from -∞ to +∞ and z from 0 to L. The K-fluorescent photon travels a distance:

$$ds = dz/\cos\theta\,, \qquad (3.3)$$

in dv, along which the reabsorption probability is $\mu_k \cdot ds$. Therefore, the Line Spread Function can be expressed as:

$$LSF(x) = \int_{-\infty}^{+\infty} \iint_0^L \frac{\mu_k \cdot e^{-\mu_k s} \cdot p(z')}{4\pi s^2} dz dz' dy', \qquad (3.4)$$

where, μ is the linear attenuation coefficient of amorphous-selenium and the distance s of a K photon travels is:

$$s^2 = x^2 + y'^2 + (z' - z)^2, \qquad (3.5)$$

and, p(z') is the probability density function that an attenuated x-ray interacts at z', which can be written as:

$$p(z') = \mu e^{-\mu(L-z')}/\eta, \qquad (3.6)$$

Where, η is the quantum efficiency of the detector:

$$\eta = 1 - e^{-\mu L}. \qquad (3.7)$$

Therefore,

$$LSF(x) = \frac{\mu\mu_k}{4\pi\eta} \int_{-\infty}^{+\infty} \iint_0^L \frac{e^{-\mu(L-z')} \cdot e^{-\mu_k s}}{s^2} dz dz' dy'. \qquad (3.8)$$

To obtain the MTF, Fourier transform is performed to the LSP, but before we perform the transformation, to simplify the calculation, some changes have been made to equation (1). First, taking $\alpha = z - z'$ and $\beta = \frac{z'+z}{2}$, we then have:

$$LSF(x) = \frac{\mu\mu_k}{4\pi\eta} \int_{-\infty}^{+\infty} \int_0^L \int_{\frac{\alpha}{2}}^{L-\frac{\alpha}{2}} \frac{e^{-\mu L} e^{\mu(\beta-\frac{\alpha}{2})} e^{-\mu_k \sqrt{r^2+\alpha^2}}}{r^2+\alpha^2} d\beta d\alpha dy', \qquad (3.9)$$

where, $r^2 = x^2 + y'^2$; we then obtain:

$$\mathrm{LSF}(x) = \frac{\mu_k}{4\pi\eta}\int_{-\infty}^{+\infty}\int_0^L \frac{e^{-\mu_k\sqrt{r^2+\alpha^2}}[1+e^{-\mu\alpha}-e^{-\mu L}-e^{-\mu(L-\alpha)}]}{r^2+\alpha^2}\,d\alpha dy'. \quad (3.10)$$

Then the Fourier transform of LSF(x) can be written as:

$$G(f) = \frac{\mu_k}{4\pi\eta}\int_0^L\iint_{-\infty}^{+\infty} \frac{e^{-\mu_k\sqrt{r^2+\alpha^2}}[1+e^{-\mu\alpha}-e^{-\mu L}-e^{-\mu(L-\alpha)}]e^{-j2\pi fx}}{r^2+\alpha^2}\,dxdy'd\alpha. \quad (3.11)$$

Let:

$$x = r\cos\varphi \qquad\qquad y' = r\sin\varphi. \quad (3.12)$$

Then the function is expressed as:

$$G(f) = \frac{\mu_k}{2\eta}\int_0^L\int_0^{+\infty} r\cdot\frac{e^{-\mu_k\sqrt{r^2+\alpha^2}}[1+e^{-\mu\alpha}-e^{-\mu L}+e^{-\mu(L-\alpha)}]}{r^2+\alpha^2}\int_0^{2\pi}\frac{e^{-j2\pi frcos\theta}}{2\pi}\,d\varphi dr d\alpha. \quad (3.13)$$

Therefore, the expression of $G(f)$ is:

$$G(f) = \frac{\mu_k}{2\eta}\int_0^L\int_0^{+\infty} \frac{e^{-\mu_k\sqrt{r^2+\alpha^2}}[1+e^{-\mu\alpha}-e^{-\mu L}+e^{-\mu(L-\alpha)}]}{r^2+\alpha^2} r\cdot J_0(2\pi fr)dr d\alpha, \quad (3.14)$$

where, J_0 is the zero order of Bessel Function, which is:

$$J_0(2\pi fr) = \int_0^{2\pi}\frac{e^{-j2\pi frcos\varphi}}{2\pi}\,d\varphi. \quad (3.15)$$

This also yields the Fourier transform at zero frequency:

$$G(0) = \frac{\mu_k}{2\eta}\int_0^L\int_0^{+\infty} \frac{e^{-\mu_k\sqrt{r^2+\alpha^2}}[1+e^{-\mu\alpha}-e^{-\mu L}-e^{-\mu(L-\alpha)}]}{r^2+\alpha^2} r dr d\alpha. \quad (3.16)$$

The MTF is unity at zero spatial frequency. Therefore, the MTF_k due to the reabsorption of k-fluorescent x-ay is:

$$MTF_k(f) = \frac{G(f)}{G(0)}. \quad (3.17)$$

3.4 The Fraction of K-Fluorescent X-Ray

When incoming x-rays initially interact with the photoconductor, the energy carried by x-ray photons will be absorbed, and the fraction of total attenuation that contributes to the photoelectric effect is f_{ph}. As we discussed, after the electrons are liberated, a characteristic fluorescent x-ray will be emitted. The possibility of emitting a fluorescent x-ray is around 60% [10]. The fraction of the reabsorbed K-fluorescent x-ray photon energy to the incident x-ray photon energy is given by [46]:

$$\rho_k = f_{ph} Y_k P_k \overline{E_k} P_r, \qquad (3.18)$$

where, P_k is the fraction of photoelectric attenuation that contributes to the incident that incoming x-ray interacts with the k-shell; Y_k is the fraction of actual K-fluorescent x-ray emitted from the K-shell interaction; $\overline{E_k}$ is the average K photon energy, and P_r is the reabsorption probability of K-fluorescent photons within the detector dimension. Table 3.1 gives the data for f_{ph}, Y_k, P_k and $\overline{E}_k$ [46].

Table 3.1 X-ray photoelectric attenuation and k-fluorescence related parameters of a-Se [46].

Average k-fluorescence energy ($\overline{E}_k$)	11.375 keV	[5]
K-shell interactional fraction (P_k)	0.88	http://physics.jnist.gov/physrefdata
Actual k-fluorescent fraction (Y_k)	0.593	[5]
f_{ph}		http://physics.jnist.gov/physrefdata

3.5 Summary

A semi-analytical model for calculating MTF due to the reabsorption of K-fluorescent x-ray photons is proposed, and the individual MTF components are discussed including the MTFs due to primary photoelectric effect, trapping and aperture. Combining all the MTF components a complete overall presampling MTF_{total} is proposed. The physics-based overall MTF model identifies the important factors that limit the x-ray image resolution of direct-conversion x-ray imaging detector system. Although the discussions are based on amorphous-Selenium photoconductors, the MTF model can be applied to other direct-conversion flat-panel x-ray imaging detectors as well, such as HgI_2, PbO and CdZnTe x-ray imaging detectors.

The proposed MTF model is applied to published data and results and conclusions will be presented in the next chapter.

Chapter 4 Results and Discussions

4.1 Introduction

In Chapter 3, an analytical overall presampling MTF model was propsed by considering each individual MTF component, including primary photoelectric effect, reabsorption of K-fluorescent x-rays, carriers trapping in the bulk and aperture for direct-conversion flat-panel x-ray imaging detector systems.

In this chapter, each MTF component will first be evaluated individually, in order to assess the component that affect the spatial resolution of the system; and then, they will be presented with different combinations. At the end, all the MTF components are included to present the overall presampling MTF of a direct-conversion flat-panel x-ray imaging detector system. These theoretical discussions of the MTF will help identify the significant factors that limit the spatial resolution of the detector, and give guidance on improving the x-ray imaging system. At the end, the accuracy of the overall presampling MTF model is evaluated. Therefore, the out put of the model is compared with published experimental data to determine this.

Note that, in this chapter amorphous-Selenium based direct-conversion flat-panel x-ray imaging detector systems are studied; therefore, all the analysis, graphs, experimental data, parameters and MTFs are all based on a-Se based detector, and all the parameters are collected and applied based on a-Se material. However, the general MTF model in this thesis can be applied to other direct-conversion x-ray imaging detectors based on other materials as well, including HgI_2, PbO and CdZnTe based direct-conversion x-ray imaging detectors.

4.2 MTF_{pe}

When the primary photoelectric effect happens, a large fraction of charge carriers are generated, and they travel away from the interaction site where incident x-ray photons first interact with atoms inside the detector. Thus, the information carried by the x-ray photons are distributed to neighbouring pixels instead of reaching a certain pixel directly. Therefore, the spatial resolution of the x-ray imaging system is degraded and that also will sacrifice the resolution of the image itself. Theoretically, the distance a primary photoelectron travels away from the initial interaction site can be assessed. The shape of the charge carriers created when they travel away is a sphere as we mentioned before, and the radius of the sphere is the average path length, which is given by Equation 2.7:

$$R_{max} = 2.76 \times 10^{-5} \times \frac{M_a E^{5/3}}{\rho Z^{8/9}} \qquad (2.7)$$

Que and Rowlands [10] estimated the relation between σ and R_{max}: $2.5\sigma \approx R_{max}$. R_{max} is related to the material and incoming x-ray energy, as it is shown in Figure 4.1. For amorphous-Selenium with incoming x-ray energies at 15 keV, 40 keV, 60 keV and 100 keV, the corresponding R_{max} is 0.002 mm, 0.103 mm, 0.0203 mm and 0.475 mm respectively.

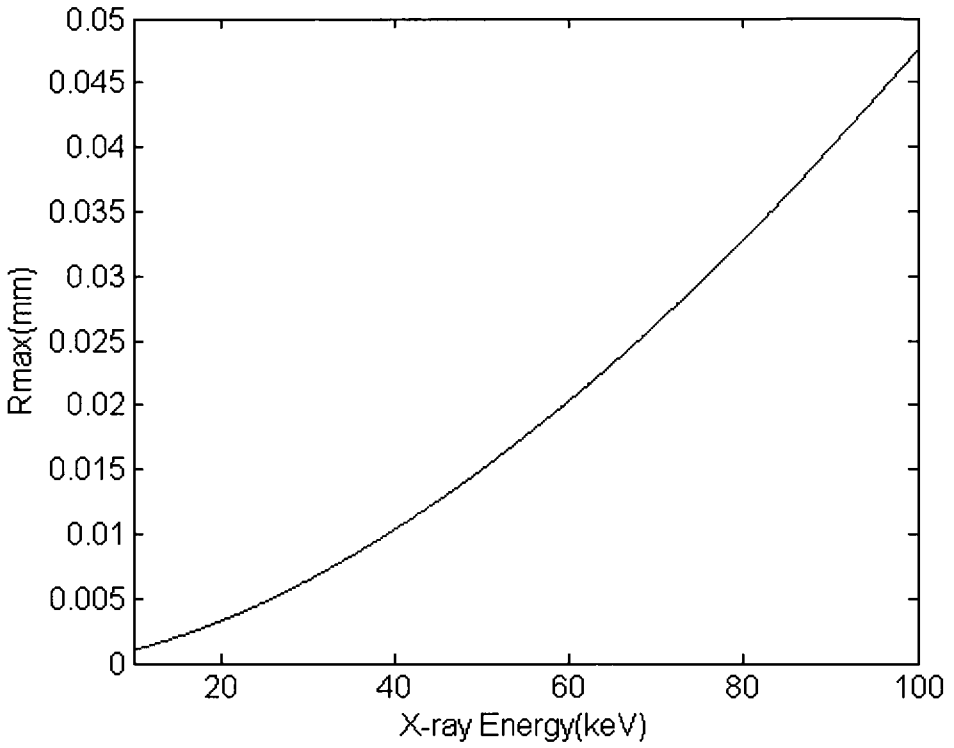

Figure 4.1 The path length (mm) of primary photoelectrons versus incoming x-ray energy (keV).

In Section 2.7, an analytical model is given to evaluate the MTF due to the primary photoelectric effect, which is shown as Equation 2.6:

$$\mathrm{MTF_{pe}} = \exp\left(-\pi^2\sigma^2 v^2\right) \qquad (2.6)$$

$\mathrm{MTF_{pe}}$ is a function of spatial frequency and σ, and because σ depends on the properties of the materials and incoming x-ray energies, for a particular x-ray imaging detector system, $\mathrm{MTF_{pe}}$ only depends on spatial frequency and incoming x-ray energy. As shown in Figure 4.2, the $\mathrm{MTF_{pe}}$ are presented versus normalized spatial frequency with different incoming x-ray energies: 15 keV, 40 keV, 60 keV and 100 keV. Note that the given normalized spatial frequency in Figure 4.2 is from 0 to 100 (lp/mm), and with

the increase of the incoming x-ray energy, the value of MTF_{pe} decreases significantly. At low x-ray energy, MTF_{pe} is extremely high, as it is shown in the figure, and when E = 15 keV, the value of MTF_{pe} is almost unity, especially for the spatial frequency range from 0 t0 20 (lp/mm). It is noticeable that when incoming x-ray energy is 100 keV, MTFpe drops dramatically at low spatial frequency.

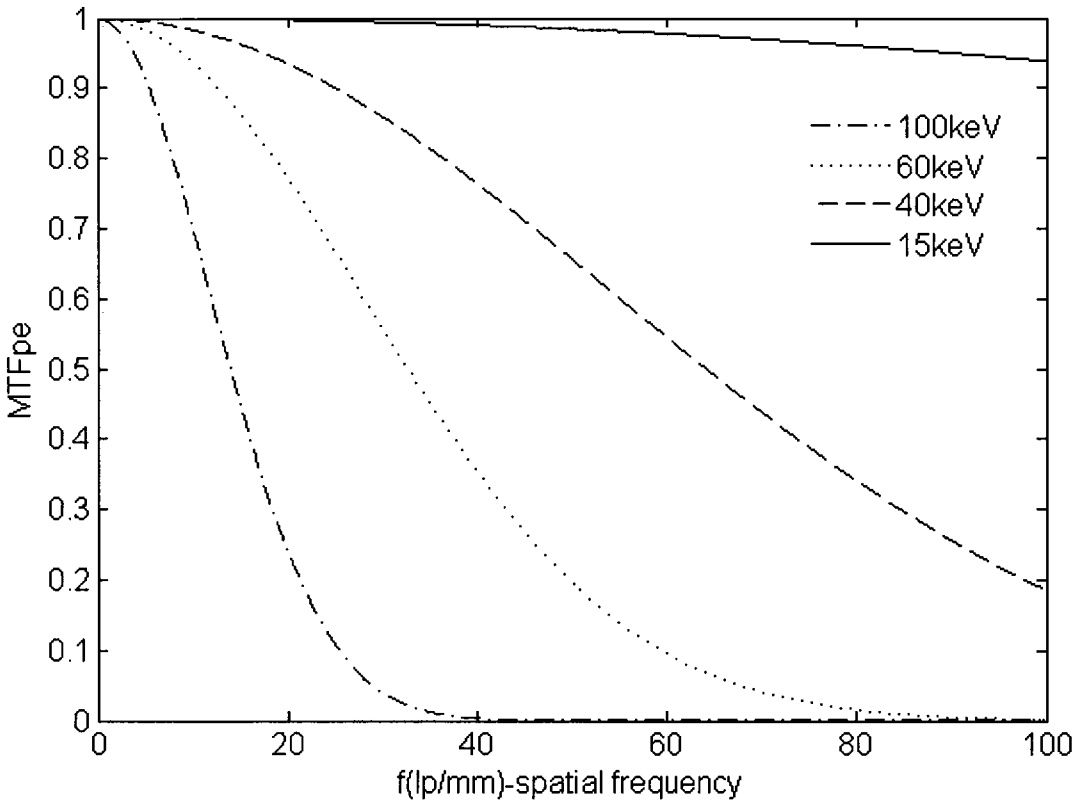

Figure 4.2 MTF_{pe} versus spatial frequency with different incoming x-ray energies.

The results indicate that MTFpe is extremely high for low incoming x-ray energy, and it is independent of the thickness of the photoconductor layer and irrelevant to the electric field applied to the photoconductor. MTFpe reduces with increasing incoming incident photon energy. The energy of the primary electron increases with increasing

incident x-ray photonic energy and thus, it moves further away from the x-ray initial interaction point and reduces the resolution.

4.3 MTF_k

The analysis, discussion and calculation of Modulation Transfer Function (MTF_k) due to the reabsorption of k-fluorescent x-rays were given in previous chapter. The primary photoelectric effect is followed by the event that k-fluorescent x-ray photons are emitted from the atoms where a cascade of electronic transitions take place. After these k-fluorescent x-ray photons are generated inside the photoconductor, they travel away from the original site and are absorbed inside the photoconductor of the detector. Because the photons are generated partial by (5% to 25%) the incoming x-ray energy which engages in the primary photoelectric effect, they carry the information of the image, and is absorbed at other sites inside the photoconductor which will degrade the spatial resolution, since the particular pixel where the information is supposed to be collected originally, will not get the same signal as the incoming x-ray photons were carrying. Thus, MTF_k is introduced to assess the spatial resolution degradation that is caused by the reabsorption of k-fluorescent x-ray.

As it can be observed from Equation 3.11:

$$G(f) = \frac{\mu_k}{4\pi\eta}\int_0^L \iint_{-\infty}^{+\infty} \frac{e^{-\mu_k\sqrt{r^2+\alpha^2}}[1+e^{-\mu\alpha}-e^{-\mu L}-e^{-\mu(L-\alpha)}]e^{-j2\pi fx}}{r^2+\alpha^2} dxdy'd\alpha \,, \quad (3.11)$$

MTF_k is a function of the photoconductor thickness L, spatial frequency *f*, linear x-ray attenuation coefficient μ and energy-absorption coefficient μ_k. The energy-absorption coefficient is a parameter that depends on the properties of the photoconductor material,

so including the photoconductor thickness, the two parameters of MTF_k are actually related to the photoconductor. However, it has been discovered that the thickness of the photoconductor does not have a significant influence on MTF_k (discussed at the end of this sectioin). The linear x-ray attenuation coefficient is a function of incoming x-ray photon energy, the value of which decreases with increasing incoming x-ray energy. This means that the higher energy incoming x-ray possess a lower chance that it will be attenuated inside the photoconductor of the x-ray imaging detector.

As presented in Figure 4.3, the MTF_k versus the normalized spatial frequency with different incoming x-ray energies is shown: 15 keV, 35 keV and 75 keV. In the figure, with the same incident x-ray energy, MTF_k decreases gradually with increasing spatial frequency *f*. When the spatial frequency is below 5 lm/pp, MTF_k drops faster, and when the spatial frequency is above 5 lm/pp, it reacts more smoothly and decreases gradually. It is also noticeable from the figure that when incoming x-ray energy is increasing, MTF_k drops which means that the resolution of the system has been degraded. At a certain spatial frequency, when energy increases from 15 keV to 35 keV, and 35 keV to 75 keV, MTF_k decreases 1% and 2% respectively, and this decrease is more noticeable when spatial frequency is above 5 lm/pp. The spreading due to K-fluorescence depends on the fluorescent x-ray energy, which is 11.375 keV. At this energy, the absorption coefficient is very high and the K-fluorescent photons are absorbed within a short distance from the primary interaction point. Therefore, it has a very little dependency on the incident photon energy.

For amorphous-Selenium (a-Se), the energies of K fluorescent x-ray photons are $E_{k\alpha}$ (11.2 keV) and $E_{k\beta}$ (12.5), and for simplicity, K_α and K_β fluorescent x-ray photons are

combined together with portions of 0.865 and 0.135 respectively. Thus, for a-Se the average energy of K fluorescent x-ray photons is $\overline{E}_k$ = 11.375 keV.

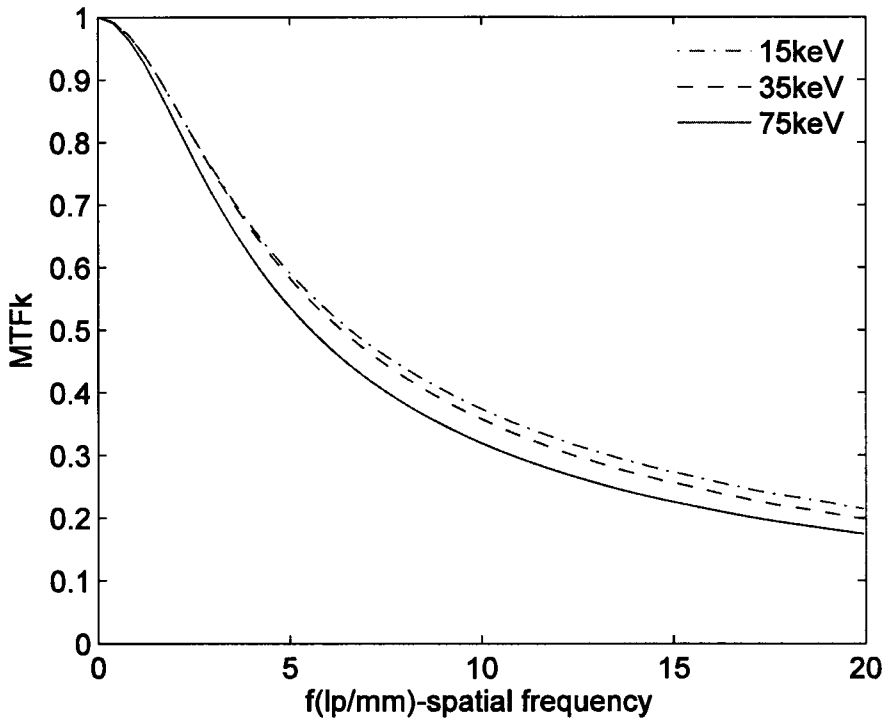

Figure 4.3 MTF_k of amorphous-Selenium based direct conversion flat-panel x-ray imaging detector, with the thickness L = 0.2 mm for incoming x-ray energies at 15 keV and 35 keV; L = 1mm for 75 keV x-ray energy.

As was mentioned earlier, the energy-absorption coefficient μ_k depends on the material and the energy of fluorescent x-ray photons. For a-Se, with an average K fluorescent x-ray photonic energy of 11.375 keV, μ_k is 14.57 (mm^{-1}). It has been discovered that the thickness of the detector does not have a significant effect on MTF_k, as plotted in Figure 4.4.

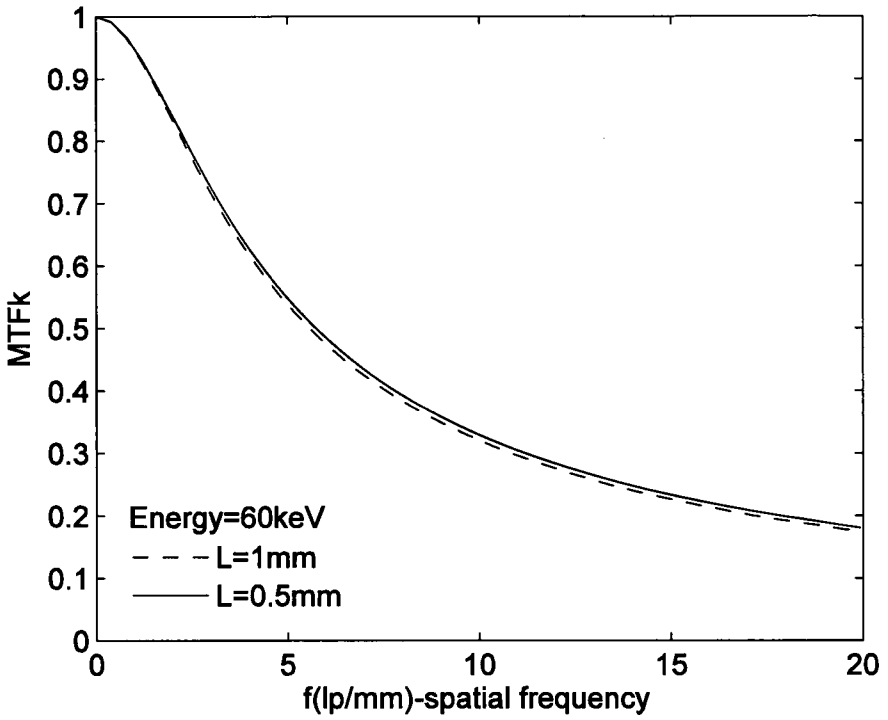

Figure 4.4 MTF_k with different detector thickness and same incident incoming x-ray energy.

4.4 MTF_w (MTF_{pe} and MTF_k)

Weighted MTF_w of MTF_{pe} and MTF_k is presented in this section:

$$MTF_w = \rho_{pe} MTF_{pe} + \rho_k MTF_k, \tag{4.1}$$

where, ρ_k is the fraction of total attenuation of incoming x-rays that contributes to the emission of K-fluorescent x-rays, which has been discussed in Chapter 3. The contribution of MTF_{pe} is approximately estimated as:

$$\rho_{pe} = 1 - \rho_k. \tag{4.2}$$

In Figure 4.5, MTF_w, MTF_{pe} and MTF_k are plotted versus spatial frequency with different incoming x-ray energies: 20 keV, 60 keV and 100 keV. MTF_k is used to evaluate the MTF due to the effect of the reabsorption of k-fluorescent x-rays, and the energy that creates the K-fluorescent x-rays are proportional to the fraction of energy that contributes to the primary photoelectric effects. Thus, theoretically the value of a weighted MTF_w of MTF_{pe} and MTF_k will be lowered by the MTF because of the reabsorption of k-fluorescent x-rays. As seen in Figure 4.5, the value of a weighted MTF with different incoming x-ray energies is shown. Note that, at low incoming x-ray energy range (~20 keV), the influence is more significant than the higher energy range. In all three graphs, it is obvious that the impact from MTF_{pe} is more considerable, since generally the fraction of MTF_{pe} is from 75% to 97% of the weighted MTF. By contrast, MTF_k has a much smaller impact on MTF_w, especially when the incoming x-ray energy is high.

It is evident from Figure 4.5 (a), (b) and (c) that the MTF_w decreases with incident x-ray photon energies, because the MTF_{pe} substantially decreases with incident photon energies.

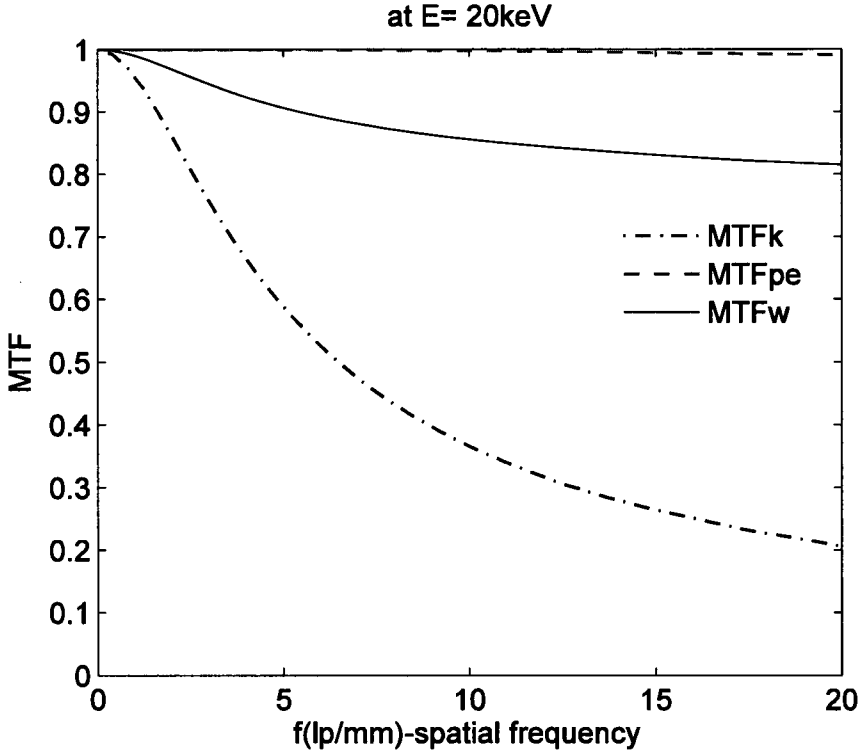
at E= 20keV
MTF
f(lp/mm)-spatial frequency
MTFk
MTFpe
MTFw
0
0.1
0.2
0.3
0.4
0.5
0.6
0.7
0.8
0.9
1
0
5
10
15
20

(a)

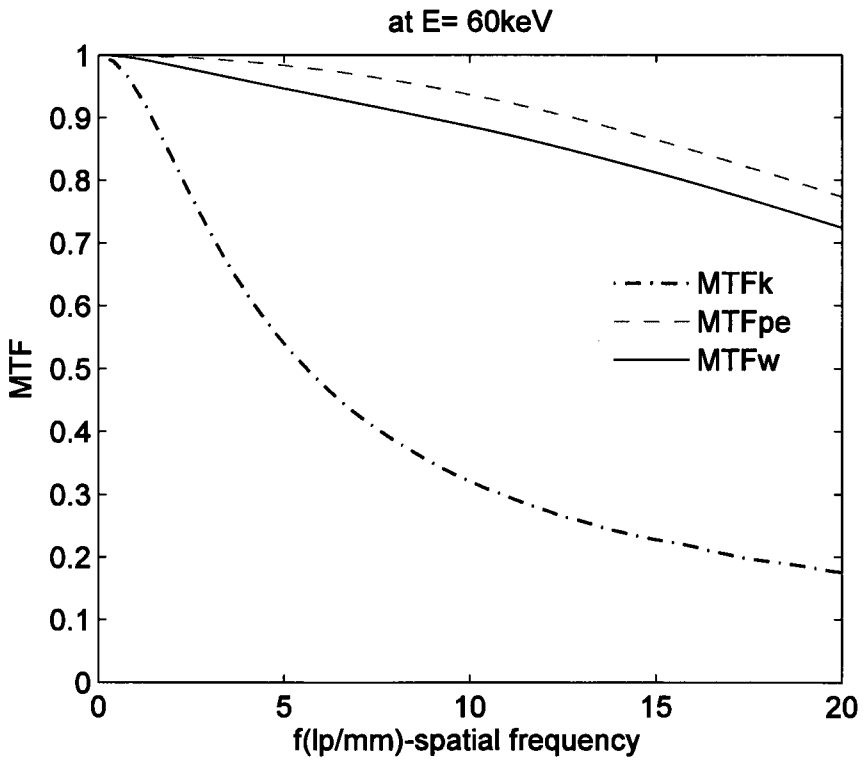
at E= 60keV
MTF
f(lp/mm)-spatial frequency
MTFk
MTFpe
MTFw
0
0.1
0.2
0.3
0.4
0.5
0.6
0.7
0.8
0.9
1
0
5
10
15
20

(b)

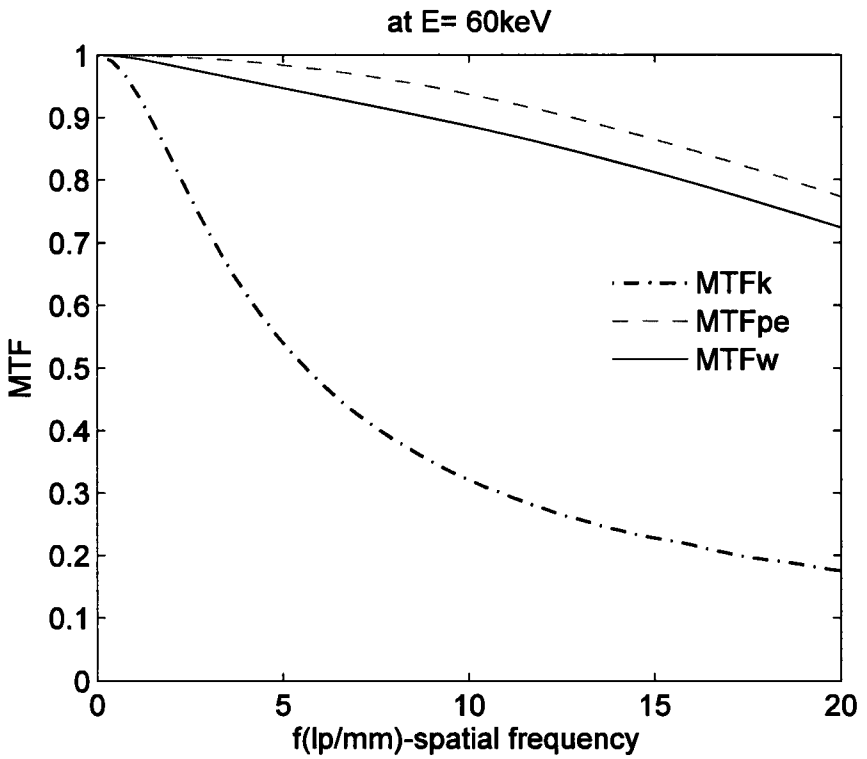

(c)

Figure 4.5 MTF_w which is weighted MTF_{pe} and MTF_k of amorphous-Selenium based direct-conversion flat-panel x-ray imaging detector system with the incoming x-ray energies at: (a) 20 keV, (b) 60 keV and (c) 100 keV (the thickness of the detector is 0.2 mm for incoming x-ray energy of 20 keV, and 1 mm for 60 keV and 100 keV).

4.5 MTF_{trap}

MTF due to trapping in an x-ray imaging detector has been discussed, and it can be calculated by Equation (2.18) which is presented in Chapter 2:

$$MTF_{trap}(f) = \frac{G(f)}{G(0)}. \qquad (2.18)$$

In Figure 4.6, MTF_{trap} versus the normalized spatial frequency are plotted. In Figure 4.6 (a), the graph describes the circumstance that the photoconductor is negatively biased and there is no carrier trapping for holes and they are all collected; on the other hand, electrons are drifted by the electric field and collected at the bottom electrode but they experience various degrees of trapping as given different values of τ_b. In (a), the curves from top to bottom represents τ_b with the values of 0, 0.3, 1, 5 and 10, respectively. As it has been discussed in Chapter 2, the effect of carrier trapping on τ_b decreases where the rate of carrier trapping increases, and the impact on MTF is as increasing rate of carrier trapping MTF_{trap} decreases. As expected, Figure 4.6 (a) shows that when τ_b decreases from 10 to 0, MTF decreases as well, especially with the values of τ_b at a lower range, where MTF_{trap} drops significantly.

In Figure 4.6 (b), MTF_{trap} are plotted versus the normalized spatial frequency with $\tau_b = \infty$ and various values of τ_t. The photoconductor is negatively biased, and all electrons are collected and holes experience various degrees of trapping when they are drifted across the photoconductor. The curves shown in (b) from bottom to top are given the values that τ_t is 0, 0.3, 1, 5 and 10 respectively. The MTF_{trap} in Figure 4.6 (b) is the opposite of the case shown in Figure 4.6 (a), because the charges collected in the neighboring pixels are the opposite of that in the radiation-receiving pixel.

Figure 4.6 (c) plots the MTF_{trap} versus normalized spatial frequency for a negatively biased detector assuming that there is no carrier trapping for holes and different level of trapping for electrons (from top to bottom, τ_b= 1, 5 and 10). Each group of MTF_{trap} has threes curves with different $\Delta = 1, 0.5, 0.25$. Within each group, as expected, when Δ increases the coresponding MTF_{trap} increases as well.

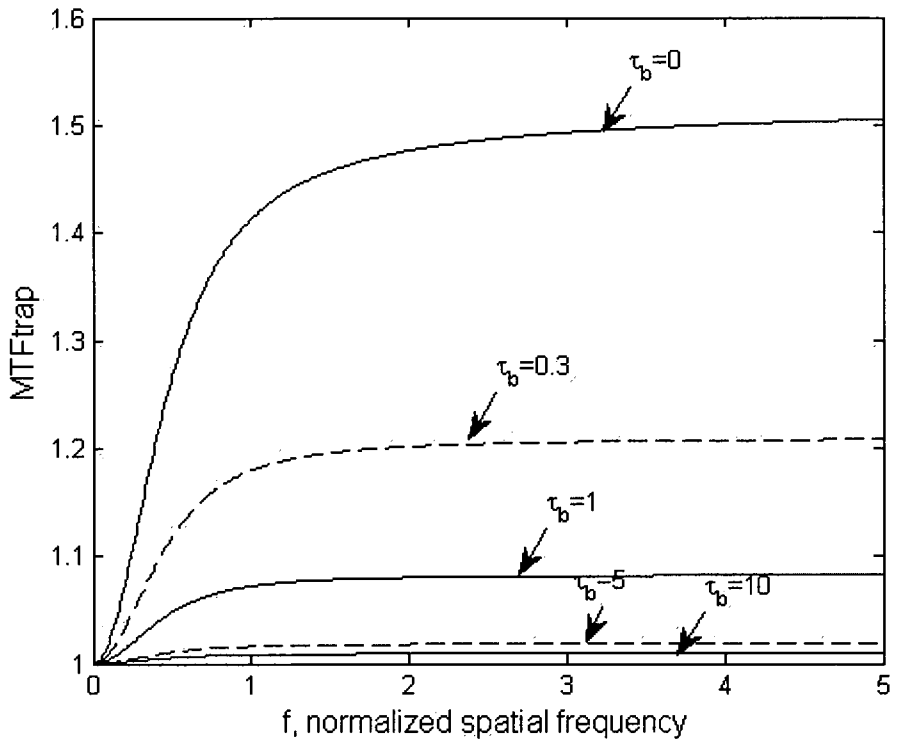

(a)

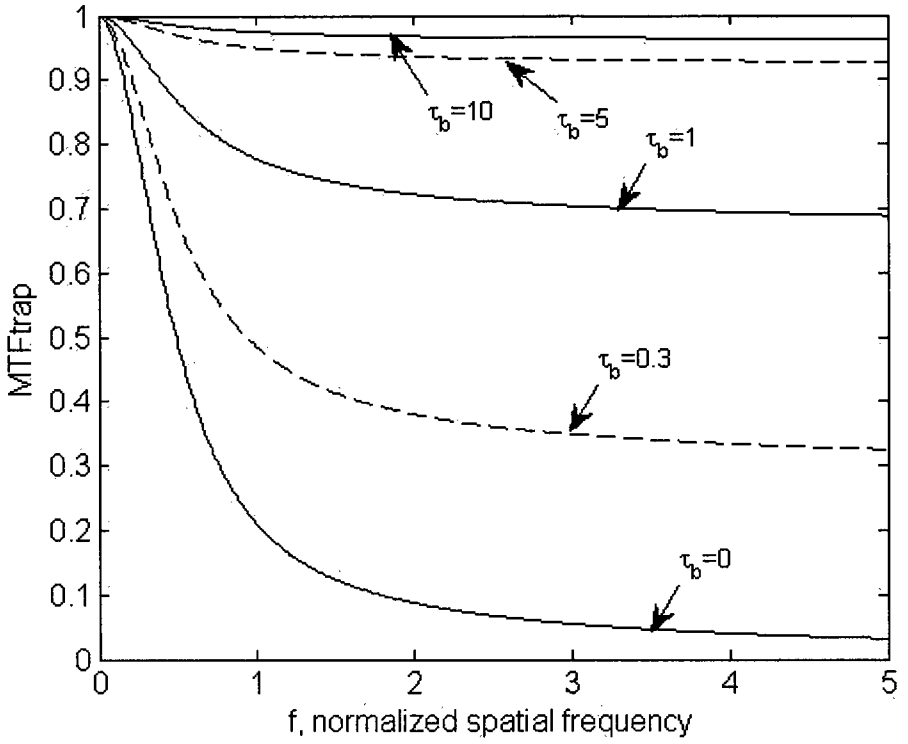
MTFtrap
f, normalized spatial frequency
τb=10
τb=5
τb=1
τb=0.3
τb=0

(b)

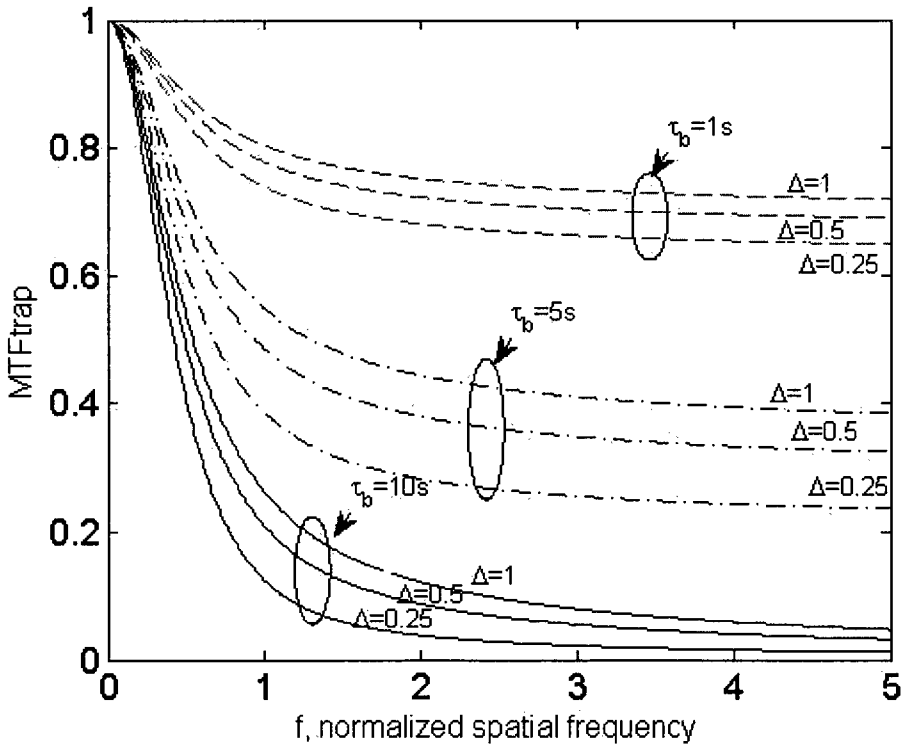
MTFtrap
f, normalized spatial frequency
τb=1s
Δ=1
Δ=0.5
Δ=0.25
τb=5s
Δ=1
Δ=0.5
Δ=0.25
τb=10s
Δ=1
Δ=0.5
Δ=0.25

(c)

Figure 4.6 (a) MTF_{trap} v.s. normalized spatial frequency with $\tau_t = \infty$ and various τ_b, when Δ is 0.5; (b) MTF_{trap} v.s. normalized spatial frequency with $\tau_b = \infty$ and various τ_t when Δ is 0.5; (c) MTF_{trap} v.s. normalized spatial frequency with $\tau_t = \infty$ and various τ_b and Δ.

4.6 MTF_{ww} (MTF_w and MTF_{trap})

Charge carriers trapping event degrades the spatial resolution of the imaging system, and our curiosity lies with the degrees of MTF_w that is affected by MTF_{trap}. The combined MTF of MTF_{trap} and MTF_w can be written as:

$$MTF_{ww} = MTF_w \times MTF_{trap}. \qquad (4.3)$$

Figure 4.7 shows the MTFs versus the spatial frequency, and each graph is plotted with different incoming x-ray energies. As shown in Figure 4.7 (a), MTF_{trap}, MTF_w and MTF_{ww} of an amorphous-Selenium based direct-conversion flat-panel x-ray imaging detector system with the photoconductor thickness of 0.2 mm and the pixel size of 0.085 mm are plotted versus spatial frequency, and incoming x-ray energy in this case is 20 keV. It is observed that MTF_w decreases as taking into consideration the MTF_{trap} and it shows that MTF_{ww} has been deducted by ~10%.

Figure 4.7 (b) shows the MTFs of the same type detector with the photoconductor thickness of 1 mm and pixel size of 0.2 mm, and the incoming x-ray energy is at E=60 keV. As it shown, the MTF_w drops significantly because of the effect of MTF_{trap}, and it is not hard to notice that, when the spatial frequency is lower than 4, MTF_{ww} declines faster as spatial frequency increases. As shown in Figure 4.7 (c), the MTFs are based on the same x-ray imaging detector as described in (b), and the only difference is the incoming

x-ray energy has been increased to 100 keV. It is noticeable that at modest and high spatial frequency range, MTF_w has more impact on MTF_{ww} than MTF_{trap}, but at lower spatial frequency range MTF_{ww} is mostly influenced by MTF_w, and it drops more significantly.

Here it has assumed that the average lifetime of electrons and holes is 10^{-3} s and 10^{-4} s for amorphous-Selenium based direct-conversion flat-panel x-ray imaging detectors.

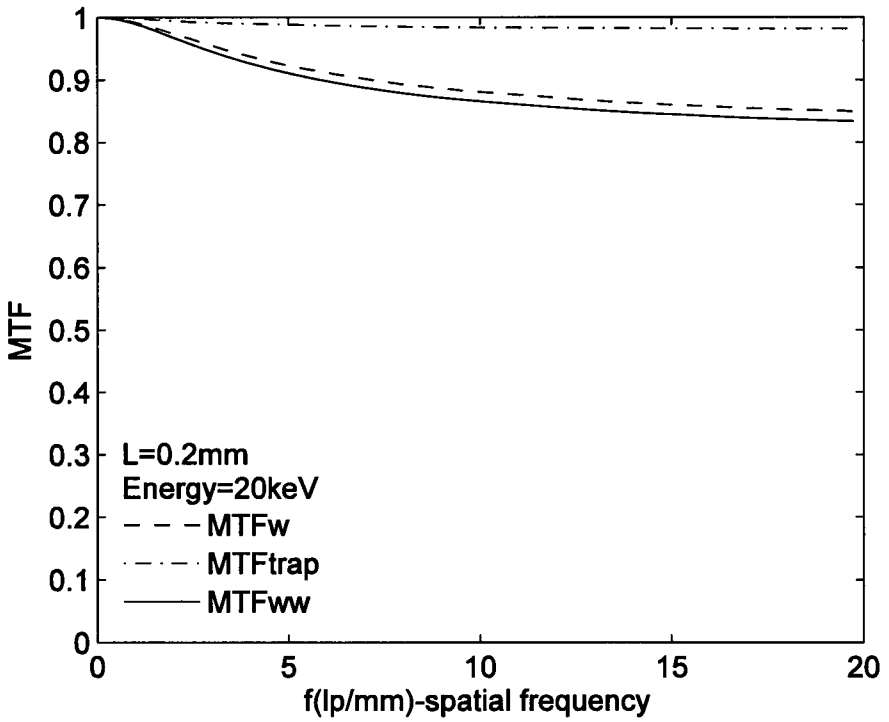

(a)

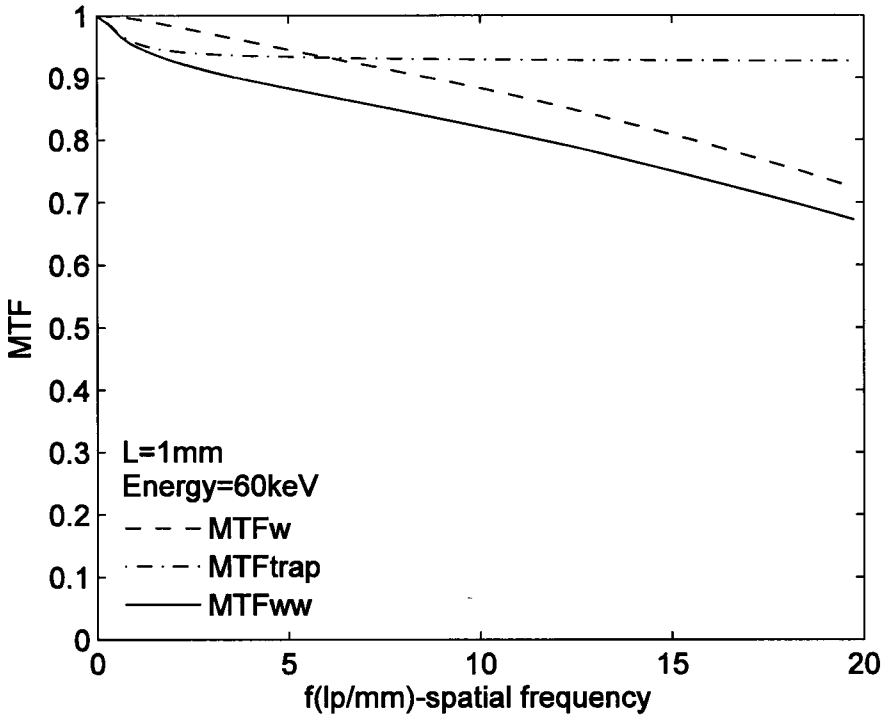
MTF
f(lp/mm)-spatial frequency
L=1mm
Energy=60keV
MTFw
MTFtrap
MTFww

(b)

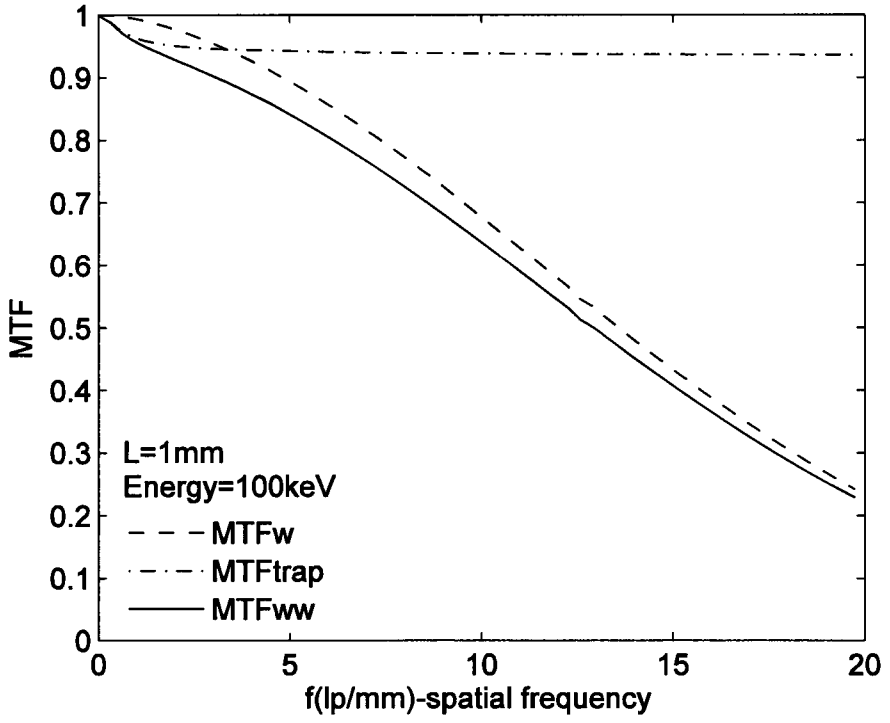
MTF
f(lp/mm)-spatial frequency
L=1mm
Energy=100keV
MTFw
MTFtrap
MTFww

(c)

Figure 4.7 MTF_{pe}, MTF_k, MTF_{trap}, MTF_w and MTF_{ww} of an amorphous-Selenium based direct-conversion flat-panel x-ray imaging detector: (a) with thickness of 0.2 mm and pixel size of 0.085 mm are plotted versus spatial frequency for incoming x-ray energy is 20 keV; (b) with 1mm detector thickness and 0.1 mm pixel size for incoming x-ray energy is 60 keV; (c) with 1mm detector thickness and 0.1 mm pixel size for incoming x-ray energy is 100 keV;

If we compare MTF_{ww} from Figure 4.7 (a), (b) and (c), it is noticeable that when the incident x-ray energy increases, the MTF_{ww} decreases as well. Especially, when we keep the same condition for the detector (set the detector thickness at L = 1 mm and α = 0.1 mm), as the incident x-ray energy increases from 60 keV to 100 keV, MTF_{ww} drops significantly.

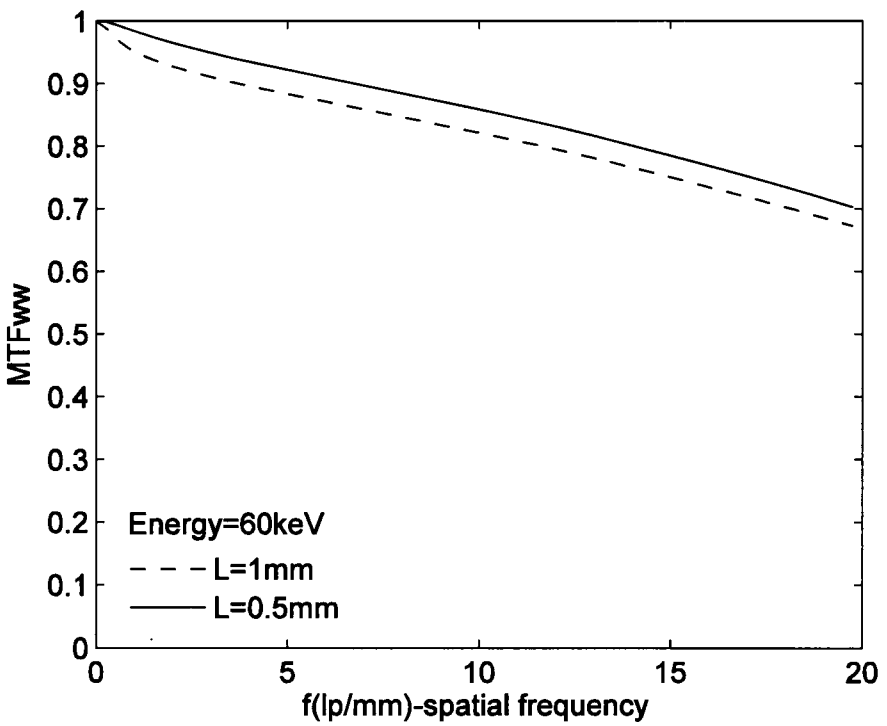

Figure 4.8 MTF_{ww} with different detector thickness and same incident incoming x-ray energy.

From previous discussion, it has been discovered that incident x-ray energy has a significant impact on the spatial resolution of x-ray imaging detectors. In contrast, with the same incident x-ray energy, the thickness of the detector has much less impact on MTF_{ww}. As it shown in Figure 4.8, when the thickness of the detector increases from 0.5 mm to 1 mm, MTF_{ww} decreases slightly (~2%).

4.7 MTF_{ap} and MTF_{total}

MTF_{ap} is considering the average signal over the area of pixel apertures and it evaluates partially the spatial resolution of an x-ray imaging detector system by describing how special frequencies pass through the apertures of the detector. Equation 2.19 in Chapter 2 gives the method to calculate MTF_{ap}, which is a function of pixel size α and spatial frequency f.

In Figure 4.9, the MTF_{ap} of amorphous-Selenium based direct-conversion flat-panel x-ray imaging detectors with the pixel size of 0.085 mm and 0.2 mm have been plotted. As expected, as the pixel size of the detector increases, the MTF_{ap} drops faster. When α = 0.2 mm, the first time MTF_{ap} becomes zero happens at spatial frequency f = 5.1 lp/mm, and by contrast that happens when f = 12 lp/mm for the same detector with the pixel size of 0.2 mm.

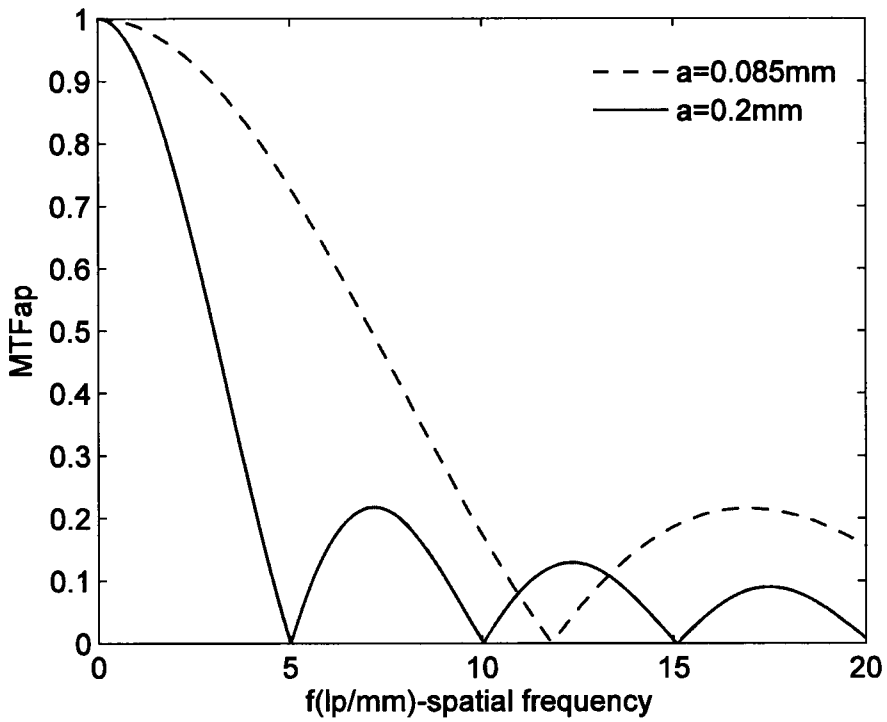

Figure 4.9 MTF_{ap} of amorphous-Selenium based direct-conversion flat-panel x-ray imaging detector with different pixel sizes.

Equantion 3.1 given in Chapter 3 is an overall presampling MTF model – MTF_{total}:

$$MTF_{total} = (\rho_{pe} MTF_{pe} + \rho_k MTF_k) \times MTF_{tr} \times MTF_{ap} , \qquad (3.1)$$

which takes the effects of the range of primary photoelectron, reabsorption of K-fluorescent x-ray photons, charge carrier trapping and aperture into consideration. It depends on the properties of the photoconductor material, incoming x-ray energy and the pixel size. Figure 4.10 shows the MTF_{total} with different incoming x-ray energies (20 keV, 30 keV, 60 keV and 100 keV), photoconductor thicknesses (0.2 mm and 1 mm) and pixel sizes (0.085 mm and 0.1 mm).

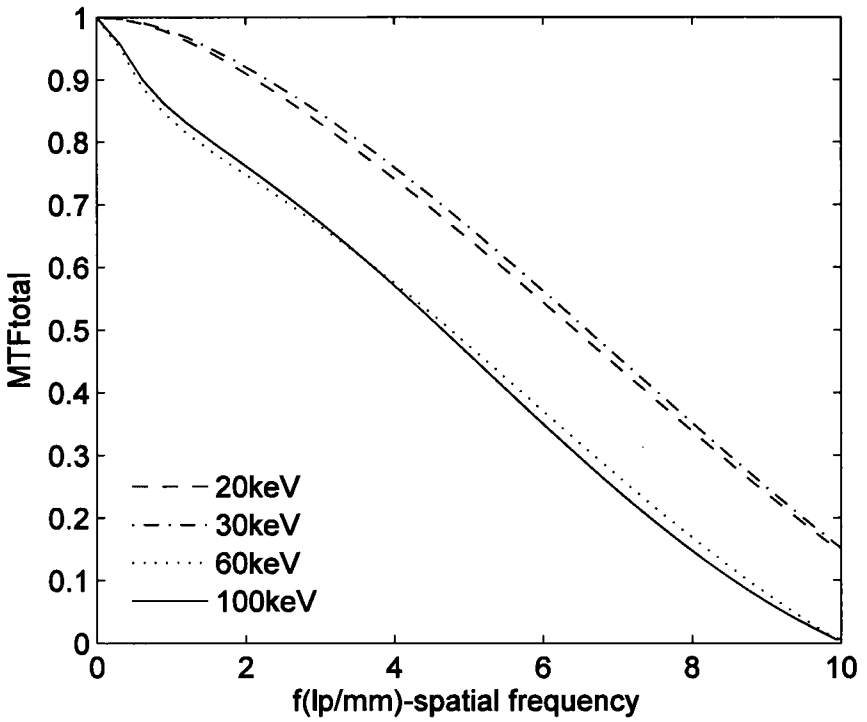

Figure 4.10 MTF_{total} of amorphous-Selenium based direct-conversion flat-panel x-ray imaging detectors with different incoming x-ray energies, thicknesses (L) and pixel sizes (α). When the incoming x-ray energy is 20 keV and 30 keV, L = 0.2 mm and α = 0.085 mm; When the incoming x-ray energy is 60 keV and 100 keV, L = 1 mm and α = 0.1 mm.

As plotted in Figure 4.10, when L = 0.2 mm and α = 0.085 mm, when we increase the incoming x-ray energy, MTF_{total} increases as well. In the figure, the x-ray energy has been increased from 20 keV to 30 keV, and it can be observed, when the x-ray energy is 30 keV, the MTF_{total} is lower than the one with 20 keV. MTF_{total} decreases steadily with increasing spatial frequency with a slop of ~1, but it is noticeable that when spatial frequency is lower than 1.5 lp/mm, the MTF_{total} decreases slower than the rest. When L = 1 mm and α = 0.1 mm, the MTF_{total} decreases with increasing spatial frequency, but

different from the previous case, it drops faster when the spatial frequency is below 1 lp/mm. The x-ray energies applied to the x-ray imaging detector system in this case are 60 keV and 100 keV, and when spatial frequency f<3.5, the detector has higher MTF_{total} with higher energy. By contrast, when spatial frequency f>3.5, the MTF_{total} of the detector is higher with higher incoming x-ray energy.

It noticeable that all the MTF_{total} plotted in Figure 4.10 have set that the electric field applied across the detector is 10^4 V/mm, and the charge carrier life time is $5x10^{-3}$ s for electrons, and $2x10^{-4}$ s for holes.

4.8 Experimental Results

The overall Modulation Transfer Function (MTF) model MTF_{total} is fitted with recently published experimental data on amorphous-Selenium (a-Se) based direct-conversion flat-panel x-ray imaging detector for different diagnostic purposes. Detailed discussions and fitting parameters are presented in the following sections.

4.8.1 Fluoroscopy

Figure 4.11 shows the comparison of the experimental presampling MTF data [23] of an a-Se based direct-conversion flat-panel x-ray imaging detector for fluoroscopy purpose with the simulation results of the overall MTF model that has been proposed in this thesis. The results from the MTF_{total} show a good agreement with the experimental data. The thickness of the detector is 1 mm and the pixel size is 1.5 mm. The top

electrode of the detector is negatively biased and the operation electric field is 10^4 V/mm. The detector is then exposed to typical fluoroscopic imaging x-ray energy. The x-ray beam is created by the x-ray tube with the potential of 75 kVp, which is approximately identical to 54 keV effective x-ray energy. To achieve the best fitting result, the electron and hole's life-time have been set to be 3.5×10^{-4} s and 8×10^{-5} s, respectively.

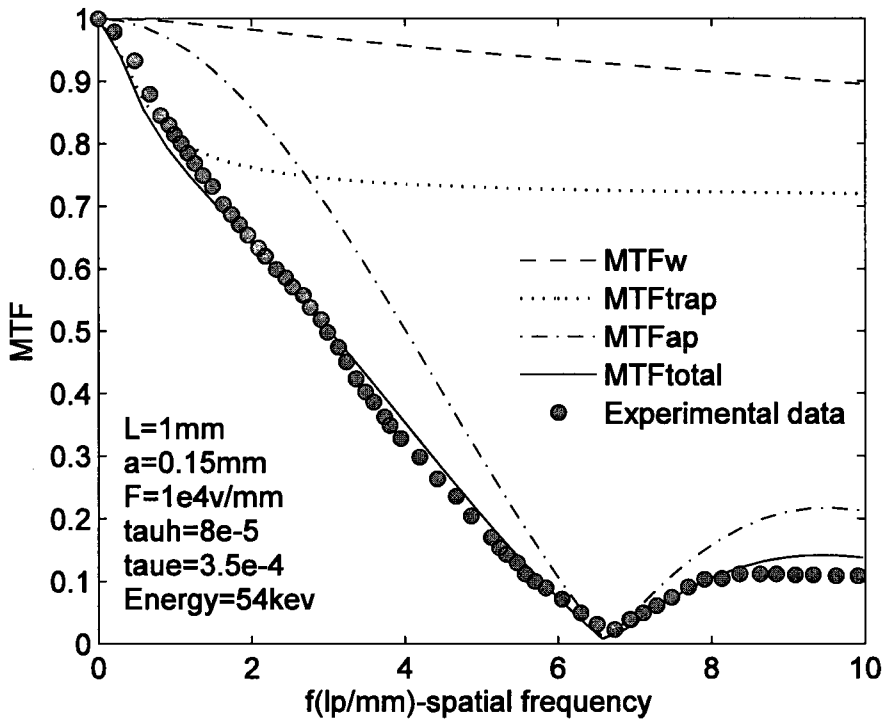

Figure 4.11 Experimental data of presampling MTF of an a-Se based direct-conversion flat-panel x-ray imaging detector in comparison with modeled results. The detector thickness is 1 mm, and pixel size is 0.15 mm. [Experimental data is taken from Ref. 23]

4.8.2 Mammography

The gate-line and data-line presampling MTF of an amorphous-Selenium based direct-conversion flat-panel prototype x-ray imaging detector is extracted from the journal paper by Zhao *et al.*[47] and is shown in Figure 4.12. The data-line direction MTF drops slightly faster than that of gate-line direction when the spatial frequency is below 6 lp/mm. The detector's thickness is 0.2 mm, and the pixel size is 0.085 mm, and it is operated with an electric field of $1.3\text{x}10^{-4}$ V/mm. The incoming x-ray is produced by using an x-ray tube with a potential of 28 kVp, and with a Molybdenum target and 30-um-thick Mo and 3.9 cm Lucite filters. The potential applied on the x-ray tube is converted into effect energy, which is 16.1 keV. In addition, the MTFs due to the range of primary photoelectrons, reabsorption of K-fluorescent x-rays, charge carrier trapping and aperture are shown in the figure in order to show how each of the components affect the overall $\text{MTF}_{\text{total}}$ which is shown in the same figure as well. The $\text{MTF}_{\text{total}}$ shows very good agreement with the experimental data. Here, in order to achieve the best fitting result, it is assumed that the electron and hole's life-time are $5\text{x}10^{-5}$ s and 10^{-6} s, respectively. It is noticeable that in comparison with other MTFs, the effect of the reabsorption of K-fluorescent x-rays and primary photoelectric effect (MTF_{w}) have a more significant influence on the overall $\text{MTF}_{\text{total}}$, and on the contrary, the range of primary photoelectrons has the least effect on $\text{MTF}_{\text{total}}$. Notice that, MTF_{w} has more influence on the total MTF when spatial frequency is lower than 2 lp/mm.

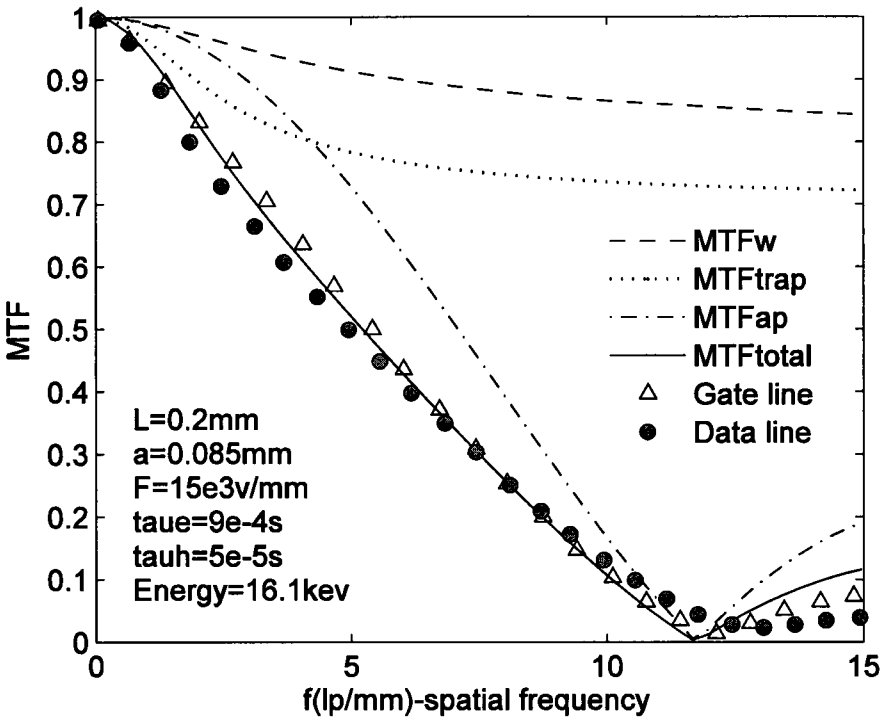

Figure 4.12 Measured presampling MTFs in data-line and gate-line direction of an amorphous-Selenium based direct-conversion flat-panel prototype x-ray imaging detector are compared with modeled results including the range of primary photoelectrons, reabsorption of K-fluorescent x-ray, charge carrier trapping and aperture as well as the overall MTF of the system - MTF_{total}. [Experimental data is taken from Ref. 47]

Figure 4.13 shows the experimental data with different x-ray energies extracted from the jurnal paper writen by Hoheisel *et al* [48]. They are compared with a simluated overall MTF_{total} of amorphous-Selenium based direct-conversion flat-panel x-ray imaging detectors for mammography. In addition, the MTFs of the range of primary photoelectrons, reabsorption of K-fluorescent x-rays, charge carrier trapping and apeture

are included as well. The simulated MTFs have a very good agreement with the measured MTFs.

In Figure 4.13 (a), the potential applied on the x-ray tube with Molybdenum anode to generate the x-ray beams is 23 kV, and the x-ray beams are filtered by a 30 um thick Molybdenum sheet. Thus the effective incoming x-ray energy used for diagnosis is evaluated as13 keV. The detector thickness is 0.25 mm and pixel size is 0.07 mm and it was operated with the electric field of 10^4 V/mm. As it can be seen, at this low incoming x-ray energy case, when the spatial frequency is above 5 lp/mm, the modeled overall MTF_{total} shows very good agreement with the measured MTF and the modeled MTF is slightly above the exprimental data at a small frequency range and also notice that the effects of MTF_w is not as significant as MTF_{ap} and MTF_{trap}. The electrons and holes' lifetime are assume to be $17x10^{-4}$ and 10^{-4} s respectively.

The measured MTF presented in Figure 4.13 (b) is from a detector with thickness of 0.25 mm, and pixel size of 0.07mm. The electric field added across the detector is 10^4 V/mm. The x-ray is then generated from a x-ray tube with Tungsten anode, a 50 um Rhodium prefilter and a 2 mm Aluminum filter are applied, and the potential applied on the tube is 28 kV. With the fitting parameters – charge carrier lifetime (electrons: $17x10^{-4}$ s and holes: 10^{-4} s), the simulated overall MTF_{total} model result shows a very good agreement with the exprimental data. However, it can be observed that in comparison to (a), the MTF_{trap} and MTF_{ap} have more influence on the MTF_{total}, and MTF_w is the dominant effect when spatial frequency is below 2 lp/mm.

In Figure 4.13 (c), the measured experimental data and modeled MTF_{total} shows a very good agreement. In this case, the experimental data was collected from the same

detector as in case (a) and (b), and the only difference is the incoming x-ray energy. Instead of applying the potential that has been used in the previous cases, the applied potential of 35 kV is applied to the x-ray generating tube with Tungsten anode, with a 50 um Rhodium prefilter and a 2 mm Aluminum filter. Therefore, the effective x-ray energy used for the imaging detector is evaluated as 22 keV. It can be noticed that at this incoming x-ray energy, MTF_w increases slightly, and it is still a dominant factor when spatial frequency is lower than 2 lp/mm. MTF_{ap} makes a significant impact on the MTF_{total} as well. The fitting parameter is the charge carrier lifetime: $2x10^{-4}$ s for electrons and 10^{-4} s for holes.

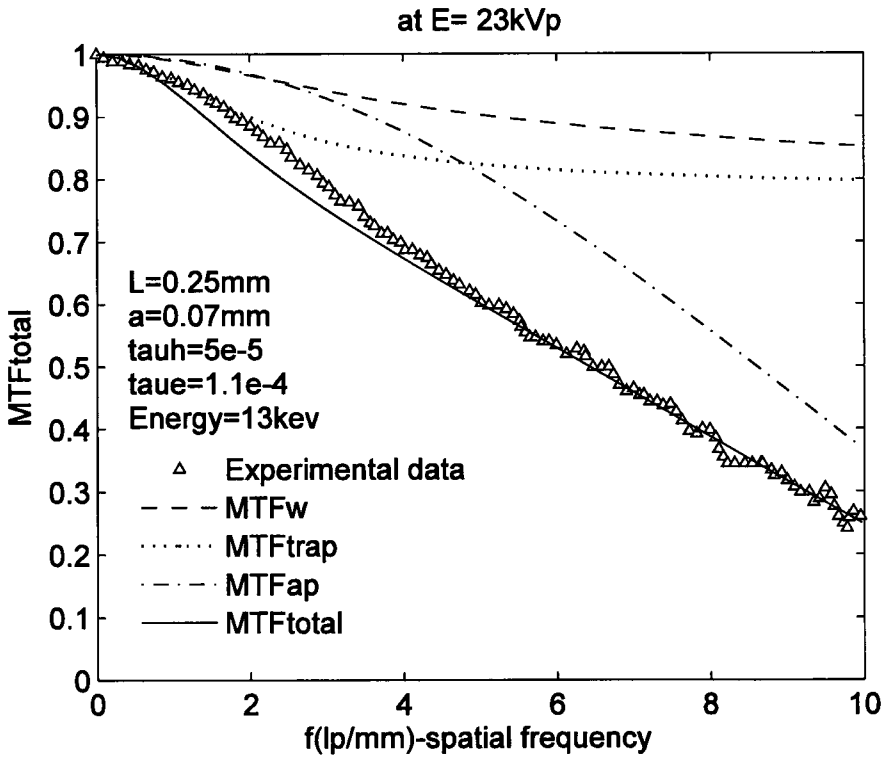

(a)

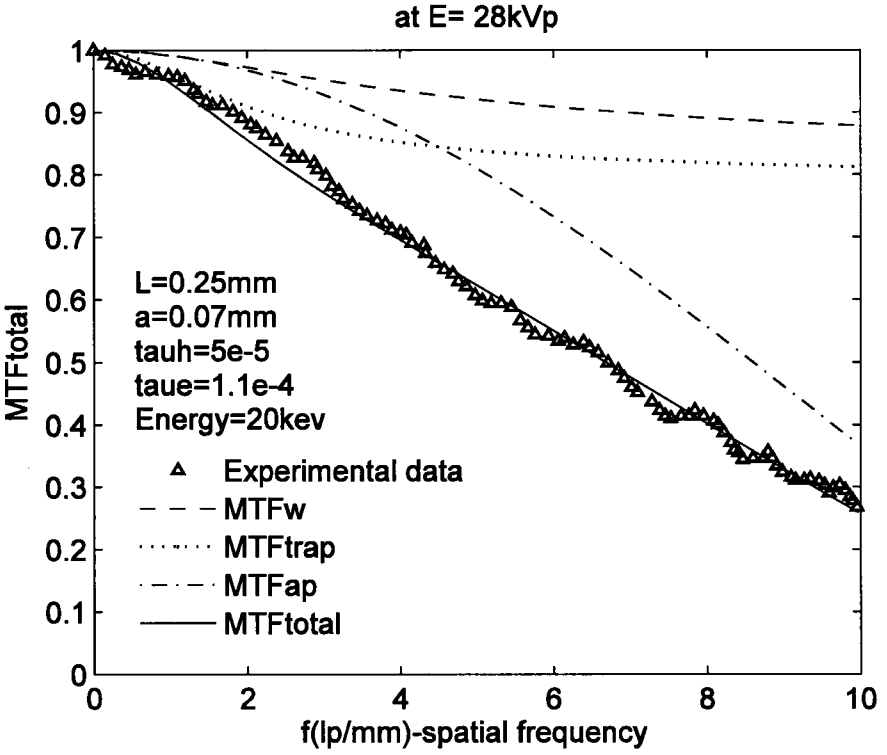
at E= 28kVp
MTFtotal
f(lp/mm)-spatial frequency
L=0.25mm
a=0.07mm
tauh=5e-5
taue=1.1e-4
Energy=20kev
Experimental data
MTFw
MTFtrap
MTFap
MTFtotal

(b)

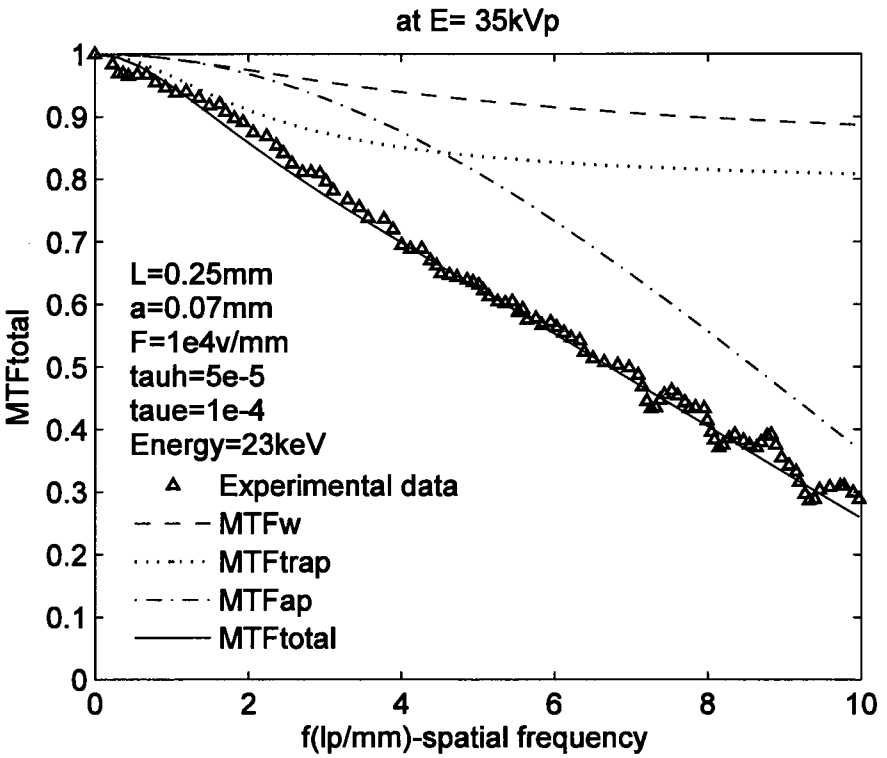
at E= 35kVp
MTFtotal
f(lp/mm)-spatial frequency
L=0.25mm
a=0.07mm
F=1e4v/mm
tauh=5e-5
taue=1e-4
Energy=23keV
Experimental data
MTFw
MTFtrap
MTFap
MTFtotal

(c)

Figure 4.13 Experimental data [48] of presampling MTF of an a-Se based direct-conversion flat-panel x-ray imaging detector (thickness is 0.25mm and pixel size is 0.07 mm) in comparison with modeled results including the range of primary photoelectrons, reabsorption of K-fluorescent x-rays, charge carrier trapping and aperture as well as the overall MTF of the system - MTF_{total}. (a) A potential of 23 kV is applied on the x-ray tube with a 30 um thick Molybdenum prefilter. (b) A potential of 28 kV is applied on the x-ray tube with a 50 um Rhodium prefilter and a 2 mm Aluminum filter. (c) A potential of 35 kV is applied on the x-ray tube with a 50 um Rhodium prefilter and a 2 mm Aluminum filter.

4.9 Summary

This chapter analyzed each MTF model with visual graphs, and then compared it to experimental data. The theoretical MTF model shows very good agreement with published experimental data.

The MTF model includes MTF_{pe}, MTF_{k}, MTF_{trap}, MTF_{ap} and overall MTF_{total} which are simulated individually and then the modeled results were compared with various published experimental data from the amorphous-Selenium based direct-conversion flat-panel x-ray imaging detectors for fluoroscopy and mammography diagnostic purposes. All the simulations are based on the corresponding x-ray imaging detectors, and reasonable fitting parameters (charge carrier life-time) were set to achieve better fitting results. The overall MTF_{total} results show very good agreement with the experimental data under various circumstances.

Chapter 5 Conclusion

The analytical overall Modulation Transfer Function - MTF_{total} of amorphous-Selenium based direct-conversion flat-panel x-ray imaging detectors is proposed in this thesis. The overall MTF_{total} includes the effects of the range of primary photoelectrons, reabsorption of K-fluorescent x-rays, charge carrier trapping and aperture. The derivations, calculations and discussions of each component and the overall MTF are presented, and the simulation results are analyzed and compared with recent published experimental data, which shows a good agreement. The overall MTF_{total} model provides the information for improving medical images quality and optimizes the dosage of the radiation on patients for various medical imaging applications.

It has been discovered that the incident incoming x-ray energy, the thickness of the photoconductor, the carrier mobility and pixel size are the key factors affecting the performance of an x-ray imaging detector system. Theoretically, the better diagnostic image of a direct-conversion flat-panel x-ray imaging detector system is achieved with lower incident incoming x-ray energy, thinner photoconductor and smaller pixel size.

5.1 Contributions

MTF is a useful tool for evaluating the performance of an x-ray imaging detector by describing the intrinsic spatial resolution of the detector. In this thesis MTFs of the range of primary photoelectrons, reabsorption of K-fluorescent x-rays, charge carrier trapping and aperture are analyzed and discussed. Each component is considered and combined in order to develop the overall MTF model.

A simpler semi-analytical expression of Modulation Transfer Function due to the reabsorption of K-fluorescent x-ray photons is proposed. Along with other MTFs of all independent stages of an x-ray imaging detector system: the stage of primary photoelectric effect (within the same stage of K-fluorescent x-ray photons' reabsorption); the stage of carrier trapping and aperture, an overall MTF model is developed.

The model can be applied to other direct-conversion flat-panel x-ray imaging detector systems as well.

5.2 Suggestions and Future Work

Most analysis, calculations and discussions presented in this thesis are based on amorphous-Selenium (a-Se) based direct-conversion flat-panel x-ray imaging detectors. The basis for my focus on these type of detectors are as follows:

1. Direct-conversion x-ray imaging detectors provide superior image quality, less cost and simpler manufacture procedures;
2. A-Se is so far one of the most used materials for direct-conversion x-ray imaging detectors due to its high x-ray sensitivity, low dark current and its ability to be easily deposited as a uniform thin film quickly to a large area.

Currently, direct-conversion flat-panel x-ray imaging detectors are the most promising methods to replace the old-fashion analog cassette films in order to digitalize radiography. Although much attention has been paid to a-Se, other materials such as poly-HgI_2, CZT and PbO are very competitive materials for x-ray detectors as well. The different properties of these materials can be applied to produce direct-conversion flat-panel x-ray imaging detectors to provide better x-ray images and reduce the x-ray dose usage on patients.

The overall MTF model presented in this thesis can be applied to polycraystalline HgI_2, Cadmium Zinc telluride (CZT) and PbO to evaluate their resolution as well.

References

[1] P. H. Hertrich, "Practical Radiography: Principles and Applications," (Wiley-VCH), pp. 12-13, (2005).

[2] L. E. Antonuk, "Electronic portal imaging devices: a review and historical perspective of contemporary technologies and research," *Phys. Med. Biol.*, **47**, R31-R65, (2002).

[3] S. O. Kasap and J. A. Rowlands, "Direct-conversion flat panel X-ray image detectors," *IEE Proc.-CDS*, **149**, pp. 85-96, (2002).

[4] E. Samei and M. J. Flynn, "An experimental comparison of detector performance for direct and indirect digital radiography systems," *Med. Phys.*, **30**, pp. 608-622, (2003).

[5] R. S. Saunders Jr., E. Samei and C. Hoeschen, "Impact of resolution and noise characteristics of digital radiographic detectors on the detectability of Lung nodules," *Med. Phys.*, **31**, pp. 1603-1613, (2004).

[6] J. A. Rowlands and S. O. Kasap, "Amorphous semiconductors usher in digital x-ray imaging," *Phys. Today*, **50**, pp. 24-30, (1997), and references therein.

[7] A. Reznik, W. Zhao, Y. Ohkawa, K. Tanioka and J. A. Rowlands, "Applications of avalanche multiplication in amorphous selenium to flat panel detectors for medical applications," *J. Mater. Sci.: Material in Electronics*, **20**, S63–S67, (2009).

[8] M. Choquette, H. Rougeote, J. Martin, L. Laperriere, Z. Shukri and B. Polischuk, "Direct selenium x-ray detector for fluoroscopy, R&F, and radiography," *Proc. SPIE*, **3977**, pp.128-136, (2002).

[9] B. Polischuk, H. Rougeote, K. Wong, A. Debrie, E. Poliquin, M. Hansrol, J. P. Martin, T. T. Truong, M. Choquette, L. Laperriere and Z. Shukri, "Direct conversion detector for digital for digital mammography," *Proc. SPIE*, **3659**, pp. 417-425, (1999).

[10] B. Zhao and W. Zhao, "Themporal performance of amorphous selenium mammography detectors," *Med. Phys.*, **32**, pp. 128-136, (2005).

[11] Z. Su, L. E. Antonuk, Y. El-Mohri, L. Hu, H. Du, A. Sawant, Y. Li, Y. Wang, J. Yamamoto and Q. Zhao, "Systematic investigation of the signal properties of polycrystalline HgI2 detectors under mammographic, radiographic, fluoroscopic and radiotherapy irradiation conditions," *Phys. Med. Biol.*, **50**, pp. 2907-2928, (2005).

[12] T. Weitkamp, C. David, O. Bunk, J. Bruder,P. Cloetens and F. Pfeiffer, " X-ray phase radiography and tomography of soft tissue using grating interferometry," *European J. Radiology,* **68**, S13–S17, (2008).

[13] S. O. Kasap, J. A. Rowlands and J. Yorkston, "Flat panel detectors for digital radiography", in Handbook of Medical Imaging, (SPIE Press, Washington, 2000), Ch. 4.

[14] M. Z. Kabir, S.O. Kasap and J.A. Rowlands, "Photocjonductors for x-ray image detectors", in *Springer Handbook of Electronic and photonic Materials*, (Springer, Heiddberg, 2006), Ch. 48.

[15] M. Kastner and D. Adler, "Valence-alternation model for localized gap states in lone-pair semiconductors," *Phys. Rev. Lett.*, **37**, pp. 1504-1507, (1976).

[16] W. C. Tan , G. Belev, K. Koughia, R.Johanson, S. K. O'Leary and S. O. Kasap, "Optical Properties Vacuum Deposited and Chlorine Doped a -Se Thin Films: Aging Effects," *J. Mater. Sci.: Materials in Electronics*, **18**, pp. 429-433, (2007).

[17] A. Carton, R. Acciavatti, J. Kuo and A. D. A. Maidment, "The effect of scatter and glare on image quality in contrast-enhanced breast imaging using an a-Si/CsI(Tl) full-field flat panel detector," *Med. Phy.*, **36**, pp. 920-928, (2009).

[18] A. R. Cowen, A. G. Davies and M. U. Sivananthan, "The design and imaging characteristics ofdynamic, solid-state, flat-panel x-ray image detectors for digital fluoroscopy and fluorography," *Clinical Radiology*, **63**, pp. 1073-1085, (2008).

[19] M. M. Wronski, A. Reznik, J. A. Rowlands, W. Zhao and J.A. Segui, "Development of a flat panel detector with avalanche gain for low-dose x-ray imaging," *Med. Phys.*, **35**, pp. 3411-3412, (2008).

[20] X. Liu, C. Lai, L. Chen, T. Han, Y. Shen, Y. Zhong, H. Zhang, Y. Yi, S. Ge, T. Wang and C. Shaw, "A-Se Flat-Panel (FP) Detector Based Scan Equalization Digital Radiography (SEDR) System: A Chest Phantom Study," *Med. Phys.* **36**, pp. 2764-2764, (2009).

[21] S. O. Kasap and J. A. Rowlands, "X-ray photoconductors and stabilized a-Se for direct conversion digital flat panel x-ray image detectors," *J. Mater. Sci.: Material in Electronics*, **11**, pp. 179, (2000).

[22] S. O. Kasap, "Photoreceptors: the selenium alloys," in *HandBook of Imaging Materials*, edited by A. S. Diamond (Marcel Dkker, New York), pp. 329-372, (1991).

[23] D. C. Hunt, O. Tousignant and J. A. Rowlands, "Evaluation of the imaging

properties of an amorphous selenium-based flat panel detector for digital fluoroscopy," *Med. Phys.*, **31**, pp. 1166-1175, (2004).

[24] D. M. Hunter, G. Belev, G. DeCrescenzo, S. O. Kasap, J. G. Mainprize, J. A. Rowlands, C. Smith, T. Tümer, V. Verpakhovski, S.Yin and M.J. YaffeThe, "The dependence of the modulation transfer function on the blocking layer thickness in amorphous selenium x-ray detectors," *Med. Phys.*, **34**, pp. 3358-3373, (2007).

[25] W. Que and J. A. Rowlands, "X-ray imaging using amorphous selenium: Inherent spatial resolution," *Med. Phys.* **22**, pp. 365-374, (1995).

[26] M. Z. Kabir and S. O. Kasap, "Modulation transfer function of photoconductive x-ray image detectors: effects of charge carrier trapping," *J. Phys. D*: *Appl. Phys.*, **36**, pp. 2352-2358, (2003).

[27] M. Z. Kabir, "Effects of charge carrier trapping on polycrystalline PbO x-ray imaging detectors," *J. Appl. Phys.*, **104**, pp. 1, (2008).

[28] Y. X. Kang, L. E. Antonuk, Y. El-Mohri, L. Hu, Y. X. Li, A. Sawant, Z. Su, Y. Wang, J. Yamamoto and Q. H. Zhao, "Examination of PbI2 and HgI2 photoconductive materials for direct detection, active matrix, flat-panel imagers for diagnostic X-ray imaging," *IEEE Trans., Nucl. Sci.*, **52**, pp. 38-45, (2005).

[29] H. Du, L. E. Antonuk, Y. El-Mohri, Q. Zhao, Z. Su, J. Yamamoto and Y. Wang, "Investigation of the signal behavior at diagnostic energies of prototype, direct detection, active matrix, flat-panel imagers incorporating polycrystalline HgI_2," *Phys. Med. Biol.*, **53**, pp. 1325-1351, (2008).

[30] J. Beutel, H. L. Kundel and R. L. V. Metter, "Handbook of Medical Imaging: Physics and psychophysics," *Volume 1 of Handbook of Medical Imaging,* (Bellingham, Washington), pp. 5-53, (2000).

[31] I. M. Blevis, D. C. Hunt and J. A. Rowlands, "Measurement of X-ray photogeneration in amorphous selenium," *J. Appl. Phys.*, **85**, pp. 7958-7963, (1999).

[32] S. O. Kasap, "*Principles of electronic materials and devices*," 2nd edition, (McGraw-Hill, New York), chapter 1, (2002).

[33] S. O. Kasap and C. Juhasz, "Time-of-flight drift mobility measurements on chlorine doped amorphous selenium films," *J. Phys. D: Appl.Phys.*, **33**, pp. 703-720, (1985).

[34] H. Z. Song, G. J. Adriaenssens, E. V. Emelianova and V. I. Arkhipov, "Distribution of gap states in amorphous selenium thin films," *Phys. Rev. B.*, **59**, pp. 10607-10613, (1999).

[35] S. O. Kasap, K. V. Koughia, B. Fogal, G. Belev and R. E. Johanson, "The influence of deposition conditions and alloying on the electronic properties of amorphous selenium," *Semiconductors*, **14**, pp. 816-821, (2003).

[36] S. O. Kasap and J. A. Rowlands, "Direct-conversion flat panel X-ray image detectors," *IEE Proc.-CDS*, **149**, pp. 85-96, (2002).

[37] R. Ning and X. Tang, "X-ray scatter correction algorithm for cone beam CT imaging," *Med. Phys.*, **31**, pp. 1195-1202, (2004).

[38] Q. Zhang, J. Rong, X. Wu, Y. Li, W. R. Chen and H. Liu, "Impacts of Filtration on Contrast-Detail Detectability of an X-ray Imaging System," *Int. J. Biomedical Imaging*, pp. 1–8, (2006).

[39] K. Kanaya and S. Okayama, "Penetration and energy-loss theory of electrons in solid targets,"*J. Phys.*, **5**, pp. 43-58, (1972).

[40] S. O. Kasap, "X-ray sensitivity of photoconductors: application to stabilized *a*-Se," *J. Phys. D: Appl. Phys.*, **33**, pp. 2853-2865, (2000).

[41] D. C. Hunt, "Imaging performance of amorphous selenium flat-panel detector for digital fluoroscopy," *SPIE Medical Imaging conference presentation*, San Diego, (2003).

[42] S. M. Seltzer, "Calculation of photon mass energy-transfer and mass energy-absorption coefficients," *Radiat. Res.*, **136**, pp. 147-170, (1993).

[43] H. P. Chan and K. Doi, "Energy and angular dependence of x-ray absorption and its effect on radiographic response in screen-film systems," *Phys. Med. Biol.*, **28**, pp. 565-579, (1983).

[44] D. R. Dance and G. Y. Day, "Escape probabilities for fluorescent x-rays," *Phys. Med. Biol.*, **30**, pp. 259-262, (1985).

[45] S. Tokuda, H. Kishihara, S. Adachi and T. Sato, "Improvement of the temporal response and output uniformity of polycrystalline CdZnTe films for high sensitivity X-ray imaging," *Proc. SPIE*, **5030**, pp. 861-870, (2003).

[46] M. Z. Kabir and S. O. Kasap, "DQE of photoconductive x-ray image detectors: application to a-Se," *J. Phys. D: Appl. Phys.*, **35**, pp. 2735-2743, (2002).

[47] W. Zhao, W. G. Ji, A. Debrie and J. A. Rowlands, "Imaging performance of amorphous selenium based flat-panel detectors for digital mammography: Characterization of a small area prototype detector," *Med. Phys.*, **30**, pp. 254-263, (2003).

[48] M. Hoheisel, L. Bätz, T. Mertelmeier, J. Giersch and A. Korn, "Modulation transfer function of a selenium-based digital mammography system," *IEEE Trans. Nucl. Sci.*, **53**, pp. 1118-1122, (2006).